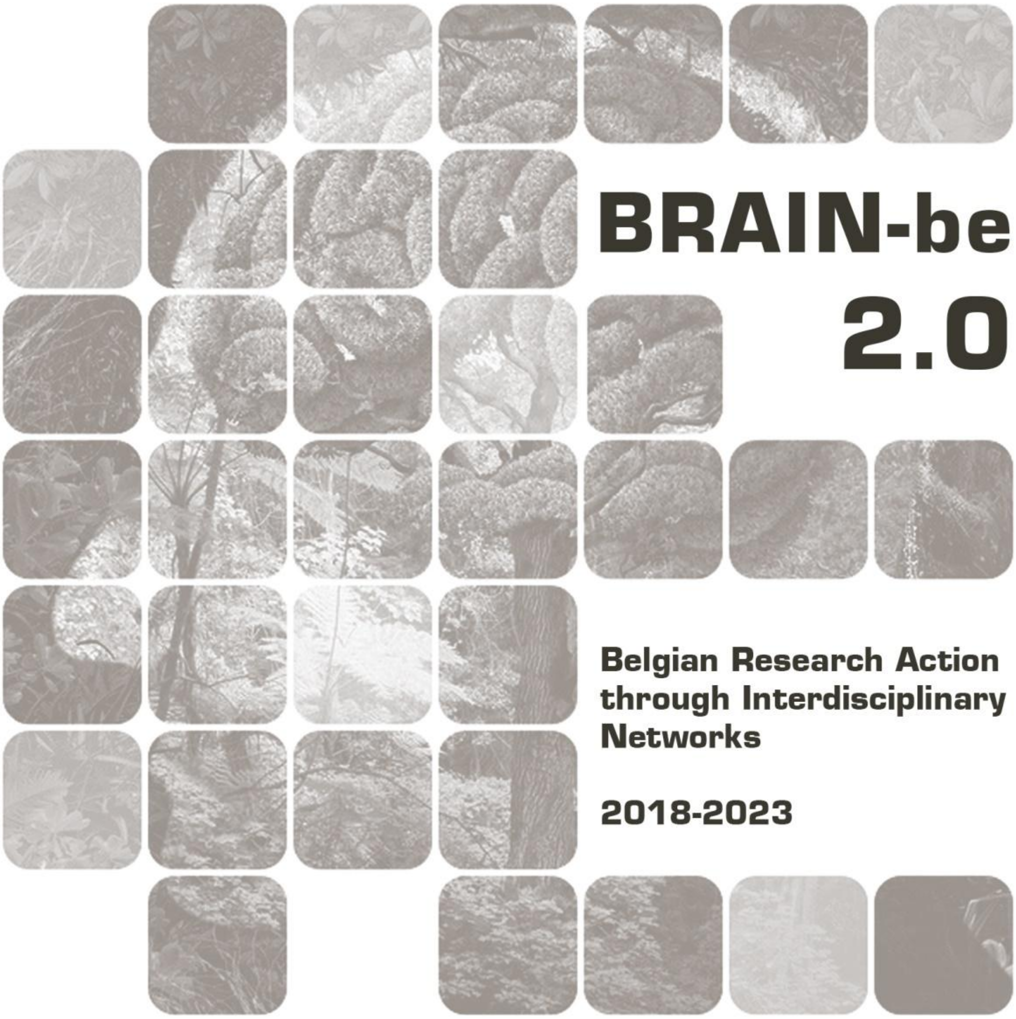

BRAIN-be
2.0

Belgian Research Action
through Interdisciplinary
Networks

2018-2023

SeVoCo

Semi-volatiles in a Comet

Frederik Dhooghe (BISA) – Johan De Keyser (BISA) – Gaël Cessateur (BISA) –
Emmanuel Jehin (ULiège)

Pillar 1: Challenges and knowledge of the living and non-living world

NETWORK PROJECT

SeVoCo
Semi-volatiles in a Comet

Contract - B2/191/P1/SeVoCo

FINAL REPORT

PROMOTORS:	Frederik Dhooghe (BISA) Johan De Keyser (BISA) Gaël Cessateur (BISA) Emmanuel Jehin (ULiège)
AUTHORS:	Frederik Dhooghe (BISA) Johan De Keyser (BISA) Gaël Cessateur (BISA) Emmanuel Jehin (ULiège)

Published in 2025 by the Belgian Science Policy Office
WTCIII
Simon Bolivarlaan 30 bus 7
Boulevard Simon Bolivar 30 bte 7
B-1000 Brussels
Belgium
Tel: +32 (0)2 238 34 11
http://www.belspo.be
http://www.belspo.be/brain-be

Contact person: Corinne Lejour
Tel: +32 (0)2 238 34 91

Dhooghe, F., De Keyser, J. Cessateur, G., Jehin, E. ***Semi-volatiles in a comet***. Final Report. Brussels: Belgian Science Policy Office 2025 – 56 p. (BRAIN-be 2.0 - (Belgian Research Action through Interdisciplinary Networks))

Table of Contents

ABSTRACT

Context: The European Space Agency's Rosetta mission visited comet 67P and examined it in great detail, in particular with the ROSINA/DFMS mass spectrometer.

Objectives: While volatile gases readily sublimate when the comet nucleus approaches the Sun, the objective of this project was to identify species that are found in small quantities only, in particular the semi-volatile compounds. Note that other instruments on Rosetta examined refractory material. To examine those lowly abundant species, the limits of the overall sensitivity of the ROSINA/DFMS measurements are pushed to the extreme by co-addition of all spectra acquired over long periods (months, up to the entire mission). However, to do this, only proper science data should be included, eliminating data which were not taken under the right circumstances, e.g. by placing constraints on the S/C orientation. A major advance in the data analysis was the establishment of a proper mass calibration technique.

Conclusions: Thanks to all these advances nurtured by the SeVoCo activities, we have been able to construct sum spectra. In this report we highlight a few of the new results concerning semi-volatiles and/or even sputtered refractories. It is now our goal to place these results in context, to examine them in more detail, and then to publish these findings.

Keywords: comets, mass spectrometry, Rosetta

1. INTRODUCTION

Comets are considered to be the most pristine bodies in our solar system. The study of comets can therefore provide information on the chemical composition of the protoplanetary disk (4.6 billion years ago) and on the role of comets in the evolution of the solar system.

A comet can be seen as an icy dirt ball describing an elliptical orbit around the Sun. As a comet approaches the Sun, the icy dirt ball (=nucleus) gets heated, and its ices progressively sublimate to form a tenuous comet atmosphere (=gas coma). Smaller grains are dragged along with the gas flow, while larger rocks and boulders fall back to or remain on the surface, which all together form a dust envelope around the nucleus (=dust coma). The grains that are released from the nucleus contain volatile, semi-volatile and refractory material. As a function of time and local grain temperature, volatile and semi-volatile material is progressively lost from the grains to the cometary atmosphere until only the refractory material remains. Rosetta, ESA's comet chaser, has studied comet 67P/Churyumov-Gerasimenko (67P in short) for over 2 years and provided a wealth of information on the nucleus and its topography, the gas coma, the dust environment, and the coma-solar wind interaction.

The SeVoCo project addresses the semi-volatiles, a group of cometary constituents which has been elusive, as none of Rosetta's instruments was specifically designed to measure them. Very little is known about these species and their importance relative to the volatile and refractory reservoirs. As such, there is no idea about their role in solar system formation and evolution and we therefore intend to learn more about these species.

As semi-volatile species are progressively released from grains, their abundance in the coma relative to the abundance of volatile species (mostly directly released from the nucleus) will increase as a function of distance from the comet. This knowledge can be applied to identify semi-volatile species in the coma. We can therefore indirectly learn more about semi-volatile compounds from the gas composition measurements of 67P obtained at variable distances from the comet (= at the spacecraft location) with the ROSINA/DFMS sensor.

The present project will use this approach to identify semi-volatile species in the coma. The sum of all identified semi-volatiles will provide a first estimation (a lower bound) of the total semi-volatile mass and its importance relative to the volatiles and refractories.

The implementation of the observations of the delayed release of semi-volatiles in our existing coma model for the behaviour of the refractory, semi-volatile and volatile components in the comet atmosphere will provide insights into how they are released into the comet atmosphere. Available ground-based observations for 67P will be used to constrain the ultimate fate of the semi-volatiles as they are photochemically processed after their release in the comet atmosphere.

2. STATE OF THE ART AND OBJECTIVES

Comets are icy bodies that originate in the outer reaches of our solar system in the Kuiper Belt or Oort Cloud. Because they spend most of their time far beyond the snow line, comets are considered the least processed bodies in the solar system since its formation 4.6 billion years ago.

A comet can be seen as an icy dirt ball describing an elliptical orbit with the Sun at its pericenter. As a comet approaches the Sun, the icy dirt ball (=nucleus) gets heated, and its ices progressively sublimate to form a tenuous comet atmosphere (=gas coma). Meanwhile, smaller grains are dragged along with the gas flow, while larger rocks and boulders fall back to or remain on the surface, together forming a dust envelope around the nucleus (=dust coma). The grains that are released from the nucleus contain volatile, semi-volatile and refractory material. As a function of time and local grain temperature, volatile and semi-volatile material is progressively lost from the grains until only the refractory material remains (Figure 1). The escaping neutral gas is ionized by the solar ultraviolet (UV) and dragged along with the interplanetary magnetic field, leading to a bluish ion tail; the grains follow the comet orbit thus forming a whitish dust tail, with the finest grains being dispersed outward by radiation pressure. These colourful tails can be observed from Earth, the reason why comets have always been an object of wonder (Figure 2).

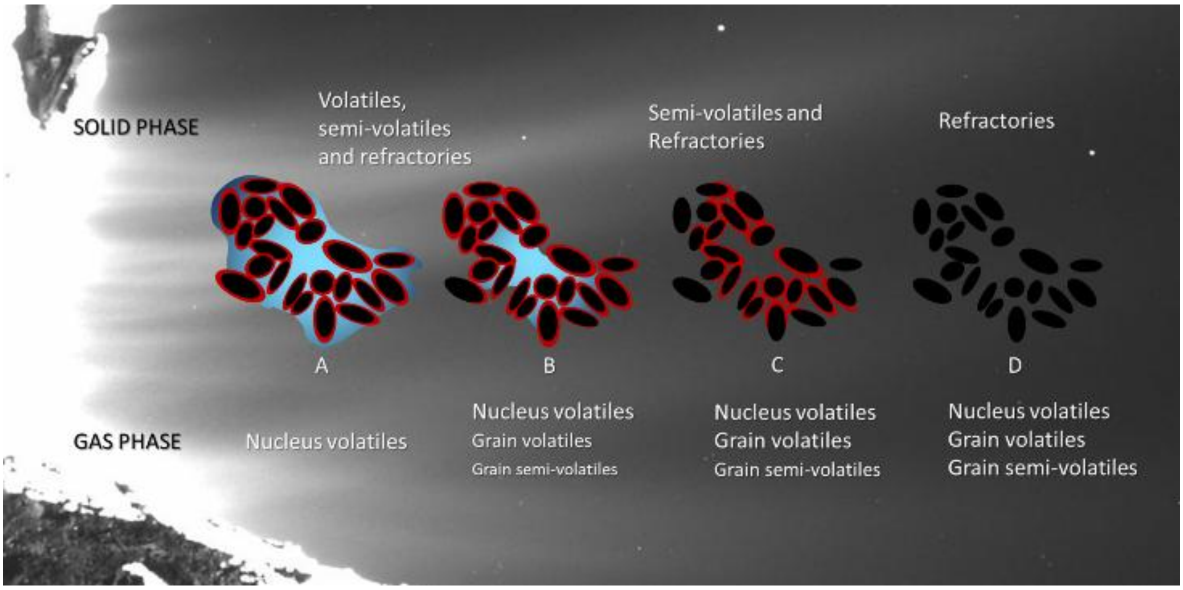

Figure 1: A to D: Schematic representation of cometary dust grain and coma evolution after nucleus release as a function of time (and local temperature)

Figure 2: Comet C/1995 O1 Hale-Bopp

In the wake of ESA's Giotto mission in 1986, after the first fly-by of comet 1P/Halley provided details on the shape, volume, and density of the nucleus as well as the coma composition, ESA initiated the Rosetta mission (Glassmeier et al., 2007). Rosetta did not perform a brief flyby but remained in the vicinity of the nucleus of comet 67P/Churyumov-Gerasimenko (67P in short) between August 2014 up to end September 2016, all the time studying the nucleus and its topography, the gas coma, the dust environment, and the coma-solar wind interaction.

BIRA-IASB contributed to build the ROSINA instrument (Rosetta Orbiter Spectrometer for Ion and Neutral Analysis, (Balsiger et al., 2007)), designed to measure the gas composition of 67P. Due to its high mass resolution, ROSINA's Double Focusing Mass Spectrometer (DFMS) allowed to measure the coma composition in unprecedented detail. This allowed the discovery of a zoo of molecules in the coma of 67P. A wealth of new insights regarding the comet itself, its formation and the early history of our Solar System, was obtained mainly by the study of the volatile species.

The SeVoCo project addresses the semi-volatile constituents in a comet. As their name suggests, the volatility of semi-volatiles is lower than these of the major coma volatile species H_2O, CO and CO_2. For semi-volatile species, information is scarce because it can be derived only indirectly from Rosetta measurements. Ground-based observations of the comet show, because of their low spatial resolution, the ultimate fate of the sum of the volatile and semi-volatile material after being photochemically processed, as well as the dust content.

Careful analysis of the rich ROSINA data set already revealed signatures of both the refractory and the semi-volatile reservoirs. When far from the sun, the solar wind was able to bombard the nucleus surface unhindered and among the sputtering products, refractory material (Si, Ca, K, Na) was detected (Wurz et al., 2015). More interestingly, the DFMS mass spectrometer provides information about the semi-volatiles. The semi-volatile release rate from the grains into the gas coma depends on cometocentric distance. As they are progressively released (Figure 3), they can be identified from DFMS spectra if the ratio of a candidate semi- volatile species to a volatile species increases as a function of distance from the nucleus. This constitutes a so-called distributed source for semi-volatile species in the coma. Because grains are dragged by the neutral gas, they move with a size-dependent speed, much slower than the ambient gas. Due to the grain speed distribution, the release of semi-volatiles will be much more uniform in latitude and longitude than the volatiles released directly from the nucleus. Consequently, the slope of the semi-volatile to volatile ratio observed during the comet's diurnal rotation decreases as a function of distance from the nucleus. Using a model of the semi-volatile release, we discovered a distributed source of semi-volatiles in the form of halogen-enriched ice (observed most clearly for Cl) (Figure 3, (De Keyser et al., 2017; Dhooghe et al., 2017). Furthermore, a very fortunate observation occurred on September 5th, 2016, at a distance of only 1.9 km above the nucleus. A large dust grain got stuck in the DFMS entrance and was heated so that its volatile and semi-volatile content sublimated over ~20 minutes and entered the mass spectrometer, providing direct composition measurements. These observations allowed a comparison of the atmosphere measurements with the Philae instruments COSAC and PTOLEMY (Altwegg et al., 2017) (volatiles + semi-volatiles). The observations during the large dust grain event led to the discovery of ammonium salts as semi-volatile material (Altwegg et al., 2020).

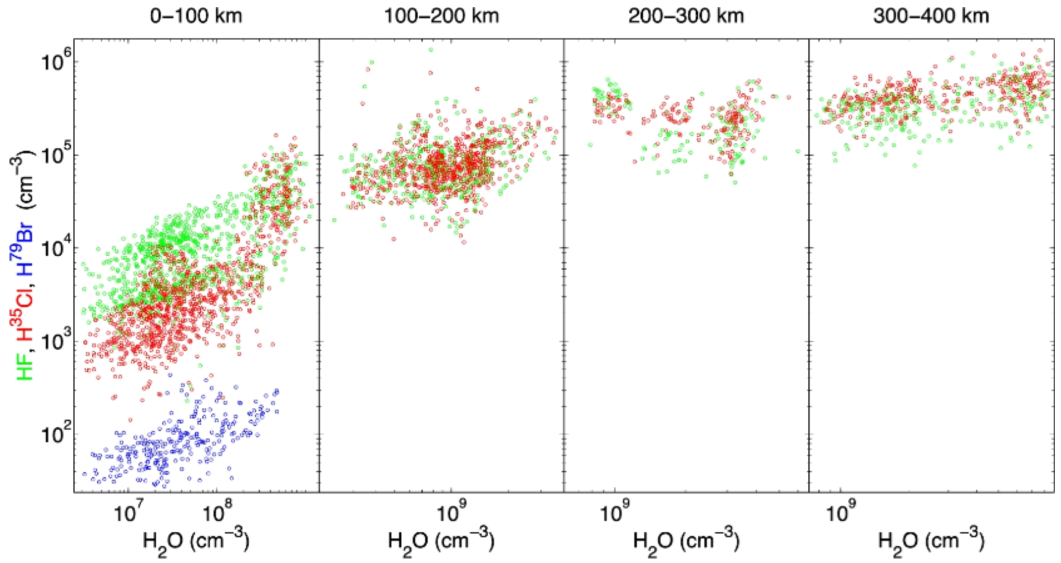

Figure 3: The correlation between HF, HCl, and HBr abundances to H2O changes as a function of spacecraft distance from the comet

The SeVoCo project aims to identify other semi-volatiles in the DFMS data in a manner similar to the one used for HCl. Summing the amounts of known semi-volatiles will allow to estimate (a lower bound on) the total semi-volatile mass and its ratio to the volatiles and refractories. This can be combined with the ice-dust ratios obtained from other instruments and also from Earth-based remote sensing observations. Studying how rapidly the semi-volatiles are released, for instance as compared to HCl, will tell us something about their distribution in the comet nucleus. Confronting observations of the delayed release of semi-volatiles with our distributed source model [De Keyser+ 2017] will provide insight into how they are released into the comet atmosphere. Finally, ground-based observations can constrain the ultimate fate of the semi-volatiles as they are photo-chemically processed in the comet atmosphere.

3. METHODOLOGY AND RESULTS

SeVoCo aimed to continue the search for semi-volatiles in the coma using DFMS data analysis in a manner similar to the one used for HCl. The indirect identification of a semi-volatile species is only possible provided the signal of possible semi-volatile candidates is sufficiently abundant so plots like Figure 3 can be created. This process is complicated by the fragmentation in the DFMS ion source, which makes it at best complicated to identify the related neutral species. Summing the amounts of known semi-volatiles will allow us to estimate (a lower bound on) the ***total semi-volatile mass*** and its ratio to the volatiles and refractories. This can be combined with the ice-dust ratios obtained from other instruments and also from Earth-based remote sensing observations. Studying how rapidly the semi-volatiles are released, for instance as compared to HCl, will tell us something about ***their distribution*** in the comet nucleus. Confronting observations of the delayed release of semi-volatiles with our distributed source model [De Keyser+ 2017] will provide insight into ***how they are released*** into the comet atmosphere. Finally, ground-based observations can constrain the ***ultimate fate*** of the semi-volatiles as they are photo-chemically processed in the comet atmosphere.

As the release of semi-volatile species from grains depends on the cometocentric distance, we need in-situ coma measurements to be able to identify and characterize them. The only applicable coma data source is the Rosetta mission to comet 67P. Particularly Rosetta's ROSINA/DFMS sensor is well suited to address this topic as it has measured the coma composition at the location of the spacecraft during the course of the mission. However, to understand how these semi-volatile species are released from grains, we also need to understand their origin: the grains. These grains contain volatile, semi-volatile and refractory material and need to be well understood. This information can be obtained from Rosetta's dust instruments. Given multiple parameters are constantly changing during the mission, a coma model which describes the behavior of semi- volatiles, volatiles and refractories is needed.

Questions to address

- Can we differentiate semi-volatiles from species emitted from nanodust?
- The 'history' of the species measured in Rosetta is lost. The only link is the location where species have been measured (S/C). A single species seen in DFMS may be linked to volatile and lesser volatile species. The paper on Fe clearly illustrates that no refractory materials are seen in Rosetta unless by surface sputtering.
- A lot of variables
    - Spacecraft related
        - Distance to the comet
        - Pointing "what are we looking at?"
        - DFMS operation and properties
    - Instrument issues

  - Relating species measured in DFMS to coma species (ionization, fragmentation, detection efficiency)
  - Dust in the instrument. How can we know when dust is being measured?
- Comet related
  - Sun-Comet distance: linked to activity and outbursts
  - Comet homogeneity?
  - Comet dynamics.

3.1. The quest for properly calibrated DFMS data

The basis of any valid scientific product is the availability and correctness of the data used and this needs a thorough and complete understanding of the operation of the measuring instrument, which will be addressed here.

3.1.1. The DFMS instrument

DFMS can sample either the ambient ions (ion modes) or the neutral gas (neutral modes), by using an electric potential barrier to block the ions from entering the instrument. Only the instrument's neutral modes without post-acceleration (no additional electrostatic potential difference between the mass analyzer exit and the detector) are considered here (mass-over-charge 13–69). A schematic diagram of the instrument is presented in Figure 4.

Neutral cometary gas enters DFMS through a 20◦ × 20◦ field-of-view aperture. A fraction of the molecules is ionized or broken up into neutral and/or charged fragments in the ion source by electron ionization, with the electrons being emitted by a filament and accelerated through a 45 V potential. The resulting ions are extracted from the source through a slit and are accelerated by a voltage V_{accel} that is chosen as a function of the mass. The analyzer has a Nier–Johnson geometry in which the charged particle beam is deflected over 90◦ by an electrostatic energy analyzer, followed by a deflection over 60◦ by a permanent magnet. Additional optical elements in the beam allow to select low or high mass resolution mode (LR/HR). These include electrostatic fields used to switch between the LR and HR slits, as well as electromagnets for the zoom optics immediately behind the magnetic sector that are used in HR mode to increase the beam dispersion. Finally, there is also the possibility to apply an electric potential between the exit of the zoom optics

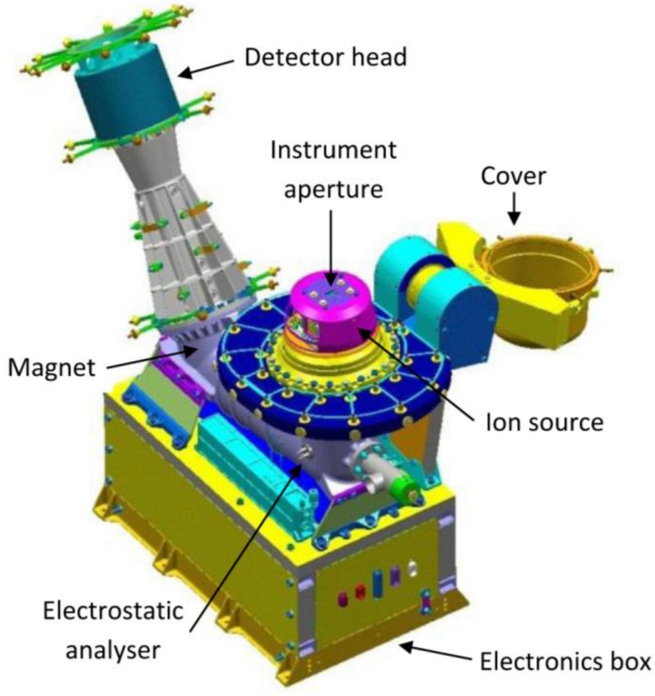

Figure 4: Schematic overview of the DFMS mass spectrometer.

and the detector to provide ‘‘post-acceleration’’ of the ions to enhance the instrument sensitivity, which is applied only for higher masses.

The resulting ion beam is usually recorded by a position-sensitive combination of a microchannel plate (MCP) with a linear CCD (the Linear Electron Detector Array or LEDA chip). The MCP consists of two layers with narrow channels in chevron configuration. Ions incident on the MCP channels create secondary electrons, which are accelerated by a static high voltage between the front and back ends of the MCP; this voltage determines the ‘‘gain’’ of the detector. As a result, an electron avalanche exits the MCP and impacts the CCD. Upon impact, these electrons can produce secondaries as well. The whole process of ion impact and secondary electron generation plays an important role in understanding how the detector ages and how one can correct for this aging. At maximum gain, 1 incident ion produces about 10^5 electrons. The LEDA chip has two parallel rows of charge collecting anodes, channels A and B. Each anode pixel can hold up to 5×10^7 electrons and is read out every 6.55 ms. The CCD output is digitized with 12 bits by an analog-to-digital converter providing a number of electron counts per pixel (1 ADC count is equivalent to 13 000 electrons), which can be translated into a number of detected ions by accounting for the secondary electron yield of the ions and the MCP characteristics.

A spectrum is built from 3000 accumulation steps for a total of 19.66 s. The MCP/LEDA combination provides two redundant 512-pixel mass spectra in an interval centered on the commanded mass-over-charge value (channel A and B). The mass resolution is around $m/\Delta m$ = 3000 in HR mode, where Δm is the full width at 1% of the mass peak height at m/z = 28. This high mass resolution has allowed the instrument to make key scientific discoveries.

Each DFMS spectrum is provided with housekeeping information which registers all instrumental settings (e.g. voltages) used and parameters measured (e.g. temperature). The commanded mass (m_c/z), the detector gain (g_{MCP}), the operation mode of DFMS and the magnet temperature (T_{mag}) largely determine the conditions at which a spectrum has been obtained. Housekeeping information is of vital importance to ensure a correct calibration.

3.1.2. Mass and intensity calibration

During the data treatment process the detector signal (ADC counts as a function of LEDA pixel number) is linked to the identity (mass calibration) and quantity (intensity calibration) of the neutral(s) entering the instrument:

- *Mass calibration (pixels → mass):* Mass calibration ideally consists of establishing a relation that associates a value of m/z with each pixel p of the LEDA array when the instrument is operated at a commanded mass-over-charge (often referred to as commanded mass or CM in short) m_c/z. Different calibration relations must be established for low- and high-resolution modes as well as for high sensitivity modes involving post-acceleration, since these modes use different settings of the electric potentials in the ion optics. The empirically established mass scale for a given spectrum for neutral HR modes without post-acceleration is

$$\frac{m}{z} = \left(\frac{m_c}{z}\right) e^{(p-p_0)(\frac{x}{ZF\,d})} \qquad \text{Eq. 1}$$

with p_0 = 256.5 pixel at the center of the detector, x = 25 µm the distance between adjacent pixel centers, d = 127 000 µm the mass dispersion, and ZF = 6.4 the dimensionless HR zoom factor. The instrument is designed so that the commanded mass-over-charge corresponds to the center of the detector, $m(p_0)/z \equiv m_c/z$. Alternatively, this can be expressed as

$$p = p_0 + \alpha \log \frac{m/z}{m_c/z} \qquad \text{Eq. 2}$$

with a dispersion factor $\alpha = ZF\,d/x$ = 32 512 pixel.

- *Intensity calibration (ADC counts → abundance of neutral species):* The calibration of the signal intensity must account for the conversion of neutrals in the ion source to ions, the conversion of the incoming ion flux by the MCP-LEDA combination into a (much larger) electron flux on the detector, which is the so-called gain, and for the conversion of the collected electrons into a digital representation.

a. ADC counts need to be corrected for the position-dependent MCP degradation according to De Keyser et al. 2019 and the offset inherent to the operation of the detector. After these corrections, the obtained values (ADC_P) represent the number of electrons collected by each pixel. ADC_P is then converted to ion counts per second and per pixel using

$$\hat{R}(p) = \frac{\mathrm{ADC}_p}{e\, g_{\mathrm{MCP}}} \frac{U_{\mathrm{ADC}} c_{\mathrm{LEDA}}}{\Delta t} \qquad \text{Eq. 3}$$

where e represents the elementary charge, g_{MCP} is the overall MCP gain factor, $U_{\mathrm{ADC}} = 2.5/(2^{12}-1)$ V is the ADC conversion factor, $c_{\mathrm{LEDA}} = 4.22 \times 10^{-12}$ F is the LEDA capacitance, and Δt = 19.66 s the total integration time.

b. For an isolated peak in a mass spectrum, the integrated area $R_Y = \sum_p \hat{R}(p)$ over all pixels that make up the peak is a measure of the number of ions Y. The number of ions of species Y that arrive at the detector is $\mathscr{R}_Y = R_Y/\mu_Y$, where μ_Y is the secondary electron yield of ion Y when hitting the MCP at the acceleration energy used in DFMS, relative to the reference species and energy. Peaks in DFMS have a double-Gaussian peak shape.

c. *Neutral densities:* Ions of species Y can be produced by ionization and/or fragmentation of several neutral parents X following

$$\mathscr{R}_Y = \sum_X n_X\, S_X f_{X\to Y}, \qquad \text{Eq. 4}$$

where n_X is the abundance of neutral species *X* and S_X is the instrument sensitivity factor for parent X. The sensitivity factor

$$S_X = \sigma_X \sum_Z \tau(m_Z) \mu_Z f_{X \to Z} \qquad \text{Eq. 5}$$

takes into account the total electron ionization (EI) cross-section σ_X of neutral species *X* in the ion source, the transmission $\tau(m_Z)$ of EI product ion *Z* through the instrument and the secondary electron yield μ_Z of product *Z* on the MCP, and where $f_{X \to Z}$ is the fraction of *Z* among the sum of all EI product ions of neutral *X*.

It is important to stress the following topics, which complicate the calibration process.

- *Non-standard and complex instrument:* DFMS is not a standard instrument and does not operate with standard settings, which means that information from existing databases with ionization information or instrument sensitivities are not (or for sure not directly) applicable to DFMS. The only correct way to obtain DFMS-specific information for neutrals is by measuring these neutrals in the instrument copy in Bern. Due to the large number of possible neutrals and the hazardous properties of some of the neutrals, this information is often not available.

- *Calibration unit:* DFMS was equipped with a gas calibration unit (GCU) holding a reference mixture containing CO_2 and the noble gases Ne and Xe with a terrestrial isotope composition to facilitate mass calibration. This provides exact mass reference points to facilitate mass calibration. However, the GCU failed before arriving at the comet. Often a priori knowledge about comet composition allows to identify a few species in a spectrum, from which a mass scale can be derived. This may not work if some species are only intermittently present above the noise level.

- *Scattered signal:* For most spectra between m/Z 13 and 69, there appears to be an unexpected additional broad signal that seems not directly related to the ions being measured. This (background) signal appears to be correlated to the intensity of neighbouring highly abundant species (e.g. H_2O, CO_2) and to m/Z. For some m/Z (e.g. m/z 21), the scattered signal obscures possible peaks in the spectrum.

- *Spacecraft background*: When measuring the neutral gas, the instrument also samples material coming from degassing of the spacecraft, from in-situ decomposition of spacecraft surface materials as a consequence of UV illumination, from the sublimation of material frozen on shadowed parts of the spacecraft (cold traps) when exposed to sunlight during spacecraft attitude changes, and from thruster exhaust (Schläppi et al., 2010). The spacecraft background must be corrected for to avoid confusion with minor constituents of cometary origin.

3.1.3. Data selection and validation

For our purposes, DFMS data for the neutral high resolution MCP/LEDA modes is used, which translates to about 1.5 million spectra theoretically usable for our purpose. Unfortunately, not all of these spectra will be usable.

Firstly, DFMS data itself can present with one or more the data issues as addressed below in illustrated in Figure 5.

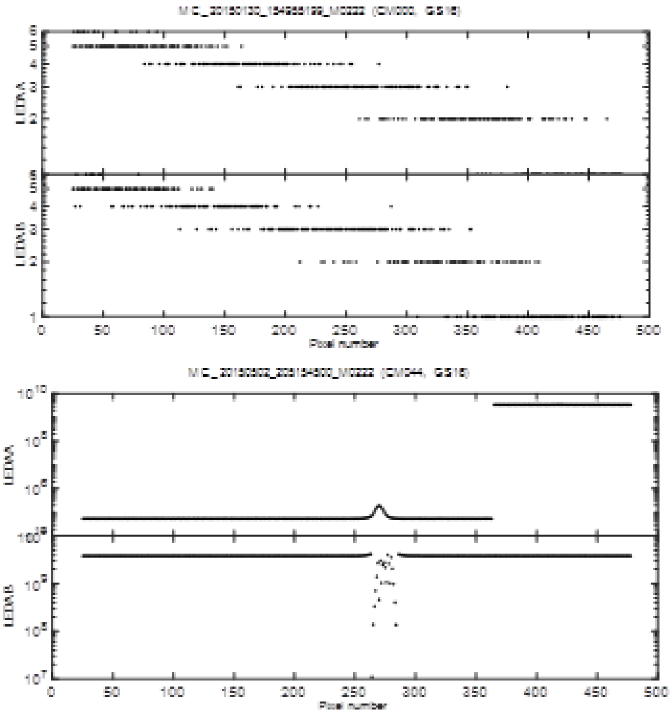

Figure 5: Illustration of DFMS data issues: Upper panel: CM0, Lower panel LEDA A: Data jump, Lower panel LEDA B: Erratic data.

- *Housekeeping issues*: Very rarely, the housekeeping registered in the file does not correspond to the spectrum itself. This is especially apparent for faulty values of the commanded mass (m_c/z), the *detector* gain (g_{MCP}), the operation mode of DFMS and the magnet temperature (T_{mag}). These spectra are to be removed.

- *CM0 data*: CM0 data are linked to instrumental offset measurements. The spectra *just* after a series of CM0 measurements always have erroneous CM values in the housekeeping. These spectra need to be removed.

- *Data jumps*: From a certain pixel on, the data signal is increased significantly by a *certain* amount (i.e., data 'jumps'). Up to two of these jumps can exist in a single spectrum and causes discontinuities. These spectra can be identified by evaluating the location of the maxima in the spectra and can be corrected for by identification and quantification of jump location and height.

- *Single pixel issues*: One or more pixels in the spectrum measure an inconsistently low signal. These spectra can be identified by evaluating the location of the minima in the spectra. Values linked to *these* pixels can be removed from the spectrum and interpolated.

- *Background issues*: for some spectra, a transient and unexpected increase of the background level is observed. Information in a spectrum at the pixel location where this increase occurs cannot *reasonably* be used to obtain information on the coma constituents. These spectra can only be identified by visual inspection.

- *Erratic data*: Any data that makes no logical sense. These spectra can be identified by evaluating the location of the maxima in the spectra *combined* with a visual inspection. These spectra need to be removed.

Secondly, when evaluating the composition of the cometary atmosphere, the data needs to be linked to coma measurements. Normally, the spacecraft observation deck points to the comet. Data for which the off-pointing angle is too large are not pointed at the comet and do not contain relevant information on neutrals coming directly from the comet.

3.2. Results and improvements

Challenges associated with lowly abundant species: It is important to note that several effects (instrumental or other) which have a negligible impact on the abundant volatile species (e.g. H_2O, CO_2, CO, O_2) can severely complicate the correct determination of low abundant species (De Keyser et al., 2019a, 2019b), such as the semi-volatiles. Within this project, considerable efforts were made to ensure the data used is of the highest possible standard. For the low abundant semi-volatile species, the signal-to-noise ratio can drastically be improved by creating sum spectra. Sum spectra are obtained by accumulation of spectra at a given m/z. The data can be accumulated for any parameter of interest (like time, Sun-comet distance, comet-spacecraft distance, …). However, this means that the individual spectra need to be mass calibrated (“aligned”) as perfectly as possible. Additional efforts were needed to correct for instrumental effects and correctly align spectra. Optimally, the pixel scale for all spectra is aligned up to 0.1 pixel.

During the project, several improvements to the data treatment process needed to be made to allow the creation of calibrated spectra and sum spectra. These improvements will be addressed here together with obtained scientific results.

- *DFMS pointing and FOV*: Depending on the altitude of Rosetta and its field-of-view (FOV), certain regions of the comet will be ‘in sight’. Note that DFMS is not an optical instrument and collects the neutrals entering the instrument. While DFMS may be pointing in a certain direction based on the available pointing information at a specific time, gas released from the nucleus at this time is actually observed in DFMS later, with a delay dependent on the gas velocity, which varies between 200-800 m/s (Lai et al., 2016), and the altitude of the spacecraft.

To be able to define possible local sources on the surface, it is necessary to identify times at which 67P is only partly in the FOV of DFMS. For about 400 000 spectra (see Figure 6, the comet is not completely in the FOV of DFMS and local features may be observed. Also, the illumination conditions of the comet play an important role. Assuming heat is efficiently absorbed at the illuminated surface regions, these regions -and layers deeper inside the comet- will be more active (i.e. release more neutral gas) relative to other regions. To illustrate and define times where local information may be obtained a routine was developed using the ESA NAVCAM shape model, Rosetta pointing and positioning information, sun position information in relation to 67P, the FOV of DFMS and its resulting 'cone of view'.

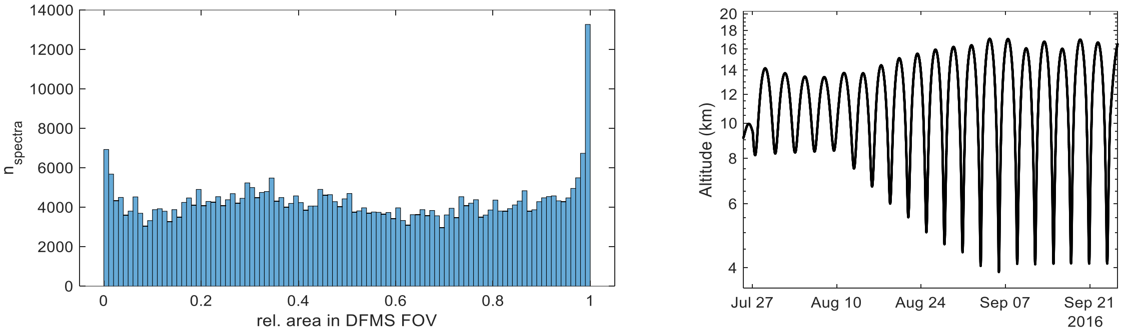

Figure 6: Left panel: Rosetta altitude above 67P. Right panel: number of spectra with a relative area between 0 and 1 in the FOV of DFMS. The values for 0 (comet outside the FOV) and 1 (comet completely in the FOV) are excluded from this histogram.

The shape model in the routine was calibrated using a series of features defined in the Cheops reference frame document (Preusker et al., 2015; Scholten et al., 2015). Some results for a series of comet orientations when the comet is not completely in the FOV of DFMS can be seen in Figure 1. The ability to compare DFMS pointing to the comet shape is of course most relevant when Rosetta was close to the comet, near the end of the mission.

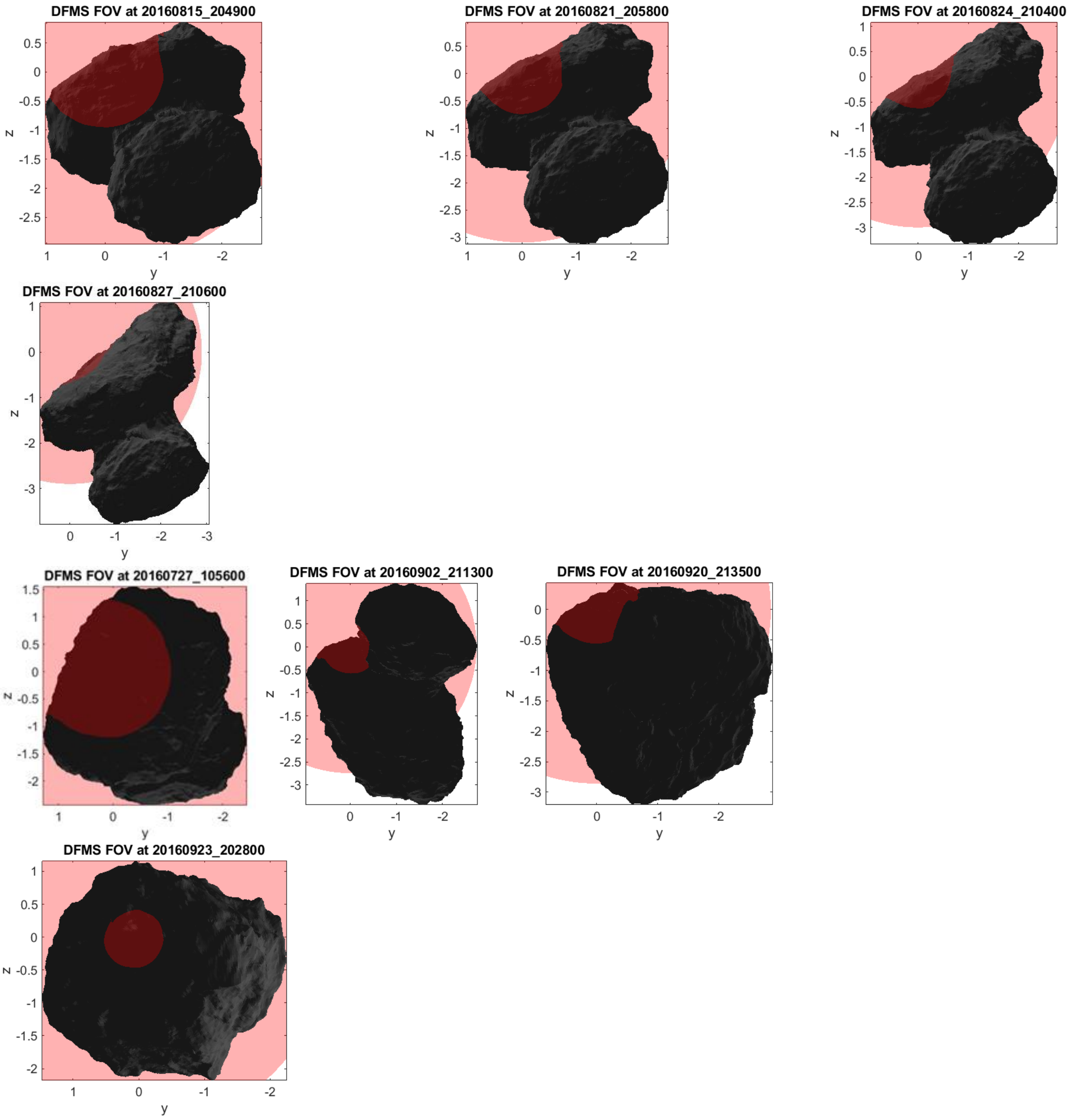

DFMS FOV at 20160815_204900

DFMS FOV at 20160821_205800

DFMS FOV at 20160824_210400

DFMS FOV at 20160827_210600

DFMS FOV at 20160727_105600

DFMS FOV at 20160902_211300

DFMS FOV at 20160920_213500

DFMS FOV at 20160923_202800

Figure 7: Area of the comet in the FOV of DFMS presented by the intersection of a FOV cone (red) and the illuminated comet (lighter gray = more illuminated). The time for each orientation is given above each plot.

- *Data selection and validation:* Problematic spectra can be detected either through inspection of individual spectra or evaluation of time profiles and back tracing. The original routines written for calibration of DFMS spectra did not have any way to identify and correct problematic spectra and made use of *daily* databases for calibration. Although this implementation is correct and robust, it had some very time-consuming limitations:

    a. Manual modification of single spectra contained in daily databases needed to identify and correct spectra with issues.

    b. Any single spectrum modification in a daily database demanded the update of the complete daily database.

c. All spectra in a daily database needed to be recalibrated after modification of any number of spectra in the database.

By itself, the identification and correction/removal of spectra with data issues is a slow process because it demands inputs from the user. Using the available implementation, the necessary time would exceed the time foreseen for the project. To optimize, a batch data treatment process was created, to gain both time and flexibility. When possible, existing routines were reused or modified.

- *Data structures for the complete mission*: new routines import LEDA data, spectra information, positioning *information*, COPS data *and* data contained within calibration files for the complete mission into separate databases which can be accessed whenever needed.

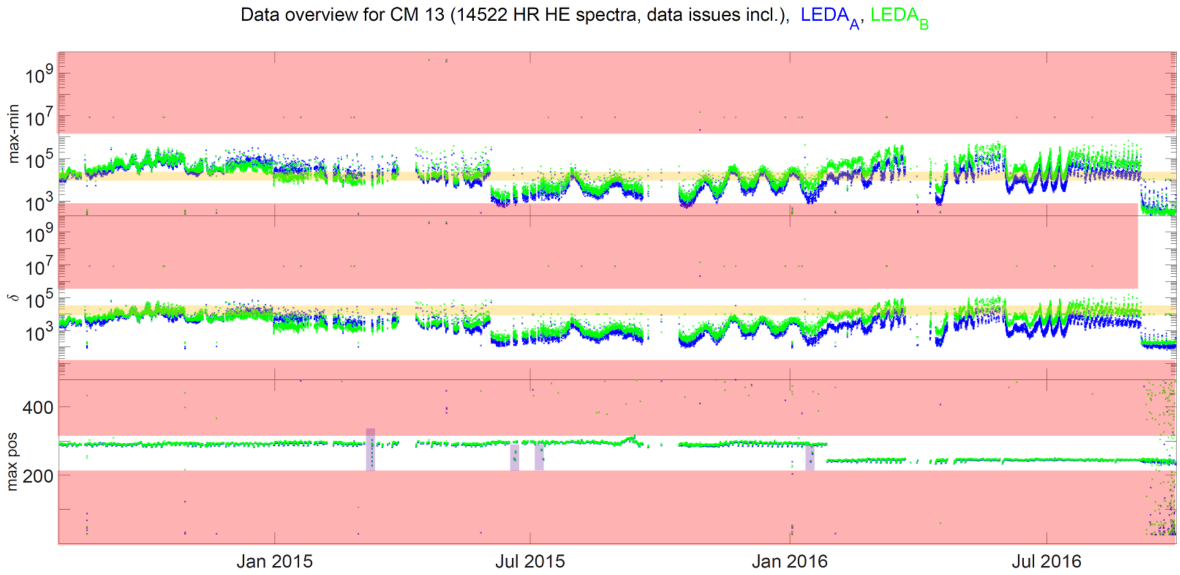

Figure 8: Mission raw data overview for CM13. Upper panel: maximum value reduced by minimum value, middle panel: maximum difference between successive LEDA pixels, bottom panel: pixel location of peak maximum. The zones coloured in red and orange indicate spectra that need to be checked manually for usability and data jumps, respectively. The zone in purple indicates spectra for which an unexpected drastic pixel shift occurs.

- *Identification and correction/removal of data issues*: for each CM, routines have been created to produce a mission *overview* for quantities *derived* from the uncorrected DFMS spectra like the maximum signal intensity and the pixel location at which maxima are found. An example for CM 13 is given in Figure 8. This allows to screen for spectra with issues and only relies on manual user inputs to define the issue type.

  A manually managed database containing all information on spectra with issues was created. New routines to correct data jumps and single pixel issues have been developed, which now allow most of previously removed data to be corrected. All corrected spectra together with their derived quantities are stored in a separate database. Corrected data can be imported from this database when needed.

The established procedures were used to identify, correct or remove spectra with data issues. This was a major achievement. For a small number of corrected spectra, the corrections produce erroneous results (< 0.1% of the spectra). Involved spectra are then categorized as erratic. Note that the methods can assist in the identification of most spectra with issues, but do not guarantee the complete removal of all spectra with issues. Validation of the data by a user therefore remains important, especially when creating sum spectra.

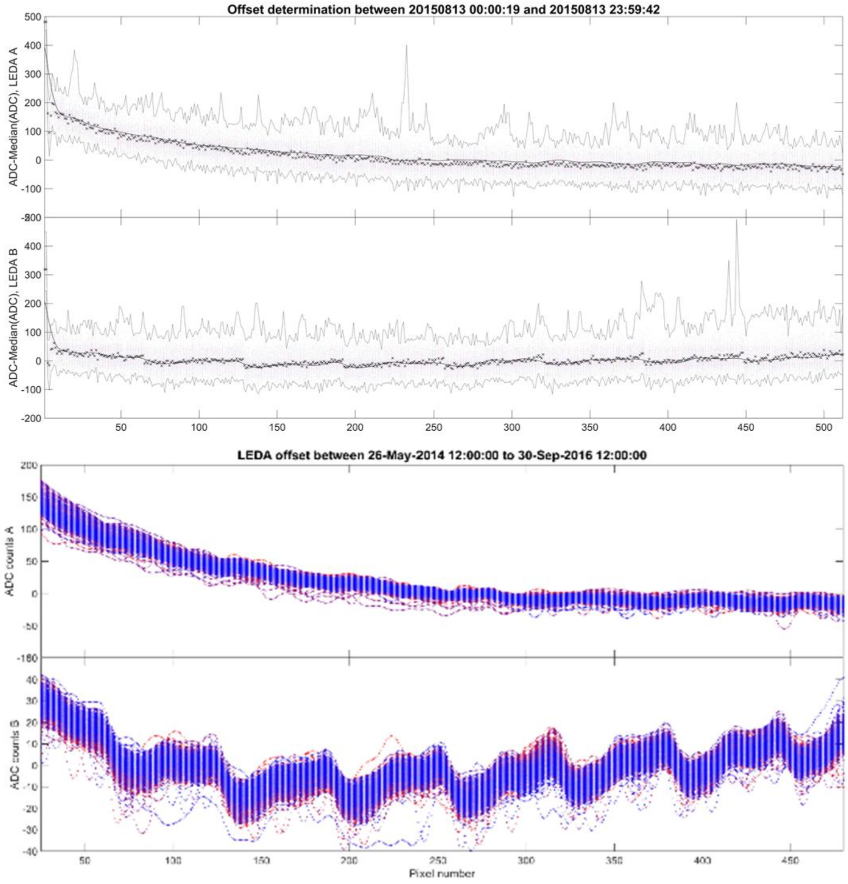

Figure 9: LEDA offset determination process for 13 August 2015 (top) and the complete mission (bottom). In the top panel, the black lines show the obtained offset.

- *Offset correction*: For species with a low abundance close to the DFMS detection limit, the LEDA offset needs to be removed correctly. To evaluate the evolution and shape of the offset, the *LEDA* offset is derived on a daily basis using data at CM 90, 95, 96, 97, 98, 99 and 100. At these commanded masses, very little signal is expected. Nevertheless, the minimum signal is smoothed with a smoothness broader than typical peaks and shifted up to the median measured offset value to remove possible peak artifacts. Although the shape of the LEDA offset is *clearly* different between both LEDA rows (see Figure 9), the offset shape for a specific LEDA row is consistent across the mission and a unique LEDA offset has been determined for each LEDA row. This LEDA offset is removed from each spectrum.

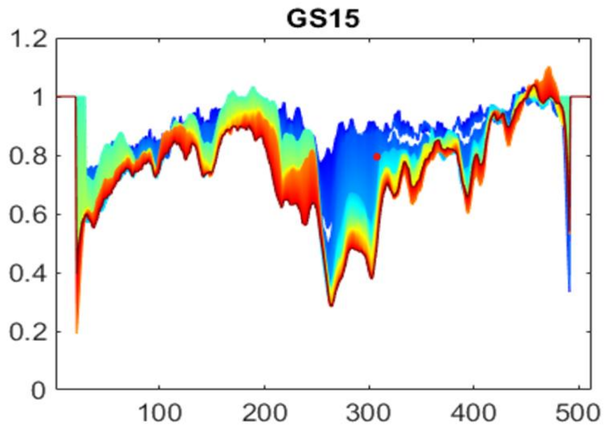

Figure 10: Illustration of LEDA A detector ageing between mission start (blue) to EOM (red)

- *Aging of the MCP/LEDA detector pixels*: Daily gain files (both overall gain and position-dependent gain) have been *determined* through interpolation of existing calibration measurements (see Figure 10), as established by (Schroeder I et al., 2019).

3.3. Chlorine-bearing species and the 37Cl/35Cl isotope ratio in the coma of comet 67P/Churyumov–Gerasimenko

The improvements in the data selection and calibration processes have opened the way to the investigation of Cl, HCl and the $^{37}Cl/^{35}Cl$ isotopic ratio in the coma for the complete mission. Results were published in Dhooghe et al. 2021 and the most important findings are presented here.

3.3.1. Data for chlorine-bearing species

The study focuses on the chlorine-bearing EI products (and a few related product ions) listed in Table 1 and shown in the example spectra in Figure 11.

Corrections applied:

- The peak area of $H^{37}Cl^+$ at m_c/z 38 was obtained by subtracting the $^{12}C^{32}S_2^{2+}$ contribution inferred from $^{12}C^{32}S_2^{2+}$ at m_c/z 78.
- The sensitivity S_X from Eq. 4 for a specific neutral X that has not been measured in the instrument copy is estimated using an approach based on the calibration for noble gases ((Calmonte, 2015), chapter 4.2.3.2), although with a high uncertainty.
- The contribution of neutrals not from the ambient coma can be considered negligible for the chlorine-bearing parent species.
- Data for which the off-pointing angle is too large are removed.
- For ratios, e.g., $^{37}Cl^+/^{35}Cl^+$, data of $^{37}Cl^+$ are associated with the closest $^{35}Cl^+$ measurement in time if their time difference is no more than 30 min (to be compared

with the ~12h comet rotation period). Data thus associated are used without any interpolation to avoid data artefacts.

Table 1: EI products at selected m/z

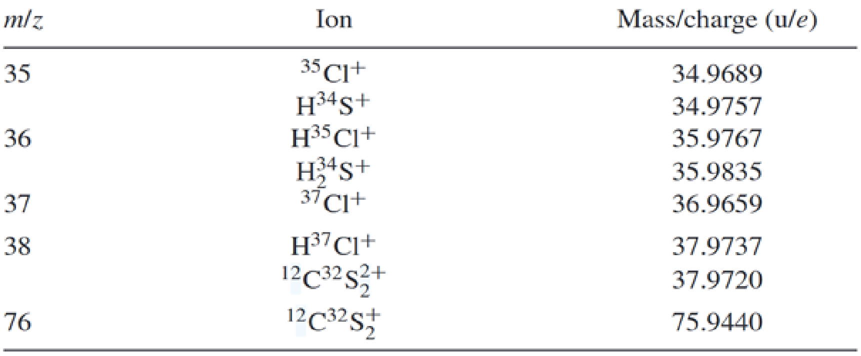

m/z	Ion	Mass/charge (u/e)
35	$^{35}Cl^+$	34.9689
	$H^{34}S^+$	34.9757
36	$H^{35}Cl^+$	35.9767
	$H_2^{34}S^+$	35.9835
37	$^{37}Cl^+$	36.9659
38	$H^{37}Cl^+$	37.9737
	$^{12}C^{32}S_2^{2+}$	37.9720
76	$^{12}C^{32}S_2^+$	75.9440

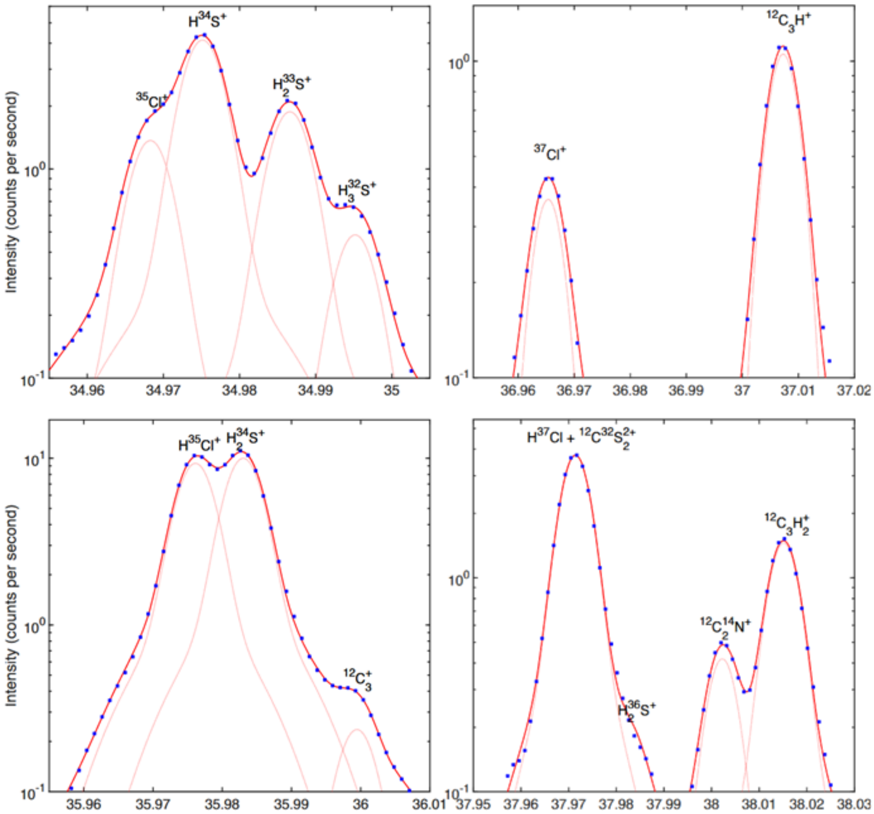

Figure 11: Sum spectra obtained by accumulation of 13 individual spectra recorded by DFMS on 11 January 2016 for mass 35 (top) to 38 (bottom) for LEDA B. The blue points represent the data, the thin dotted curves the fitted contributions of different ions, and the red curve the sum of all contributions.

3.3.2. Determination of isotope ratios

The use of ratios has the advantage that some of the parameters from Eq. 4 do not need to be exactly known. In the paper, the ratios for all parameters of Eq. 4 and Eq. 5 are addressed in detail and a thorough error analysis on all ratios is presented. It is important to note that the ratio of the integrated areas (R) need to be corrected for the remaining differences in transmission (τ) and secondary ion yields (μ) between isotopes to obtain the correct isotopic ratio based on the number of ions and their derived neutrals; for the Cl isotope ratio in HCl, for instance, one has

$$\frac{n_{H\,^{37}Cl}}{n_{H\,^{35}Cl}} = \frac{\mathcal{R}_{H\,^{37}Cl}}{\mathcal{R}_{H\,^{35}Cl}} = \frac{\tau_{H\,^{37}Cl}}{\tau_{H\,^{35}Cl}} \frac{\mu_{H\,^{37}Cl}}{\mu_{H\,^{35}Cl}} \frac{R_{H\,^{37}Cl}}{R_{H\,^{35}Cl}} \qquad \text{Eq. 6}$$

The isotope ratio is established from measurements over a prolonged time period by taking a weighted logarithmic average. Logarithmic averaging is used to compute average ratios, which is the most appropriate manner since it treats uncertainties on numerator and denominator on an equal footing. In addition, weighted averaging can account for the range of uncertainties on individual measurements. Measurements with higher count rates and thus a lower Poisson uncertainty have a larger weight in determining the average. In determining the uncertainty on this average, the random error due to Poisson counting statistics decreases as the number of measurements increases.

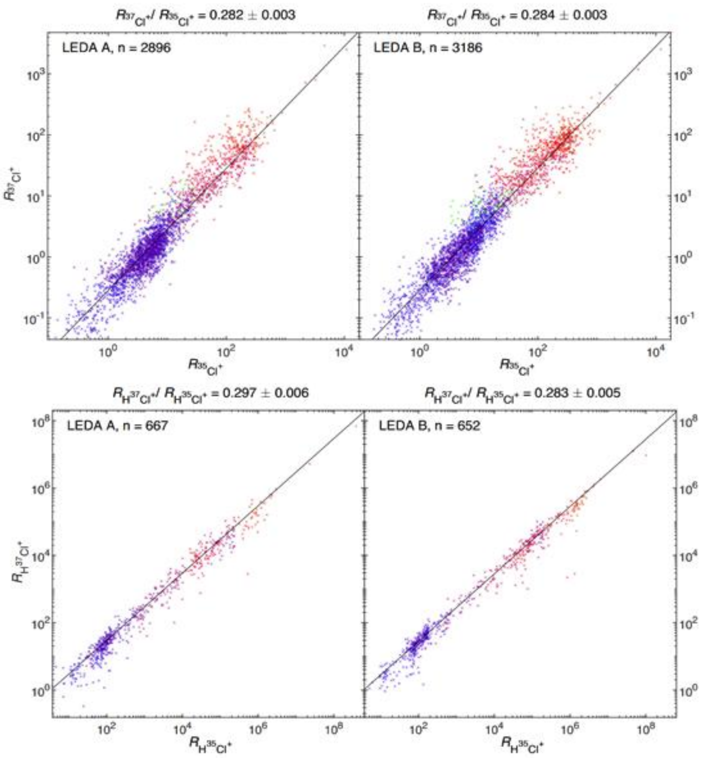

Figure 12: Upper panel: R_{37Cl+} as a function of R_{35Cl+}, lower panel: R_{H37Cl+} as a function of R_{H35Cl+}. The weighted logarithmic average isotope ratio is given by the black line and its value and uncertainty are presented above the plot.

The ^{37}Cl/^{35}Cl isotope ratio from the weighted average of the Cl and HCl measurements are presented in Figure 12 and summarized in Table 2.

1. The data are scattered evenly around the line representing the weighted average during the whole time period, which implies that the ^{37}Cl/^{35}Cl isotope ratio does not change significantly throughout the mission.

2 The logarithmically weighted time averages for $^{37}Cl/^{35}Cl$ and $H^{37}Cl/H^{35}Cl$ for both LEDA channels and the complete data set are compatible with each other within the random error margin.

3 When combining all obtained results, the overall $^{37}Cl/^{35}Cl$ isotope ratio for the coma is 0.336 ± 0.017.

4 The $\delta^{37}Cl$ value of the coma of 67P is 51 ± 55 and is in agreement (1.0σ) with SMOC and most other Solar system bodies.

Table 2: $^{37}Cl/^{35}Cl$ isotope ratios obtained using integrated areas (R) and number of ions ($\mathcal{R}$) together with random (δR) and total ($\delta\mathcal{R}$) 1σ uncertainties and number of spectra used (n).

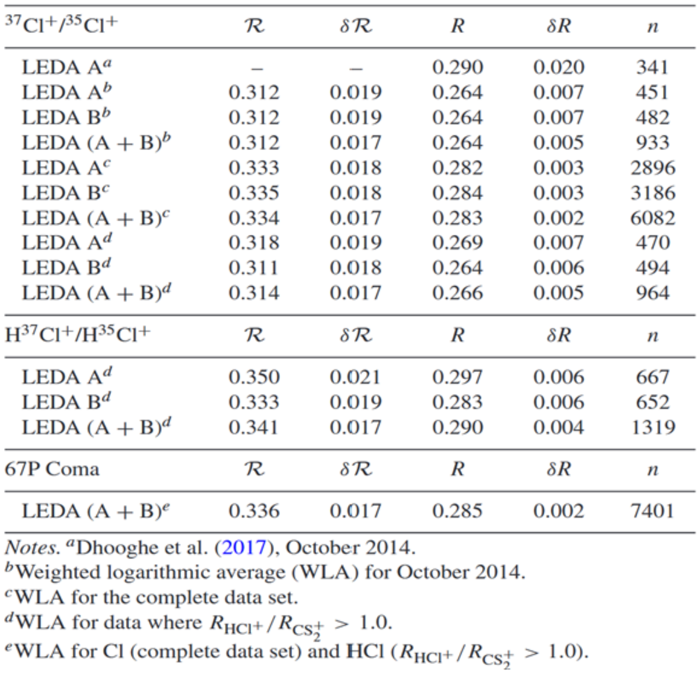

$^{37}Cl^+/^{35}Cl^+$	$\mathcal{R}$	$\delta\mathcal{R}$	R	δR	n
LEDA A[a]	–	–	0.290	0.020	341
LEDA A[b]	0.312	0.019	0.264	0.007	451
LEDA B[b]	0.312	0.019	0.264	0.007	482
LEDA (A + B)[b]	0.312	0.017	0.264	0.005	933
LEDA A[c]	0.333	0.018	0.282	0.003	2896
LEDA B[c]	0.335	0.018	0.284	0.003	3186
LEDA (A + B)[c]	0.334	0.017	0.283	0.002	6082
LEDA A[d]	0.318	0.019	0.269	0.007	470
LEDA B[d]	0.311	0.018	0.264	0.006	494
LEDA (A + B)[d]	0.314	0.017	0.266	0.005	964
$H^{37}Cl^+/H^{35}Cl^+$	$\mathcal{R}$	$\delta\mathcal{R}$	R	δR	n
LEDA A[d]	0.350	0.021	0.297	0.006	667
LEDA B[d]	0.333	0.019	0.283	0.006	652
LEDA (A + B)[d]	0.341	0.017	0.290	0.004	1319
67P Coma	$\mathcal{R}$	$\delta\mathcal{R}$	R	δR	n
LEDA (A + B)[e]	0.336	0.017	0.285	0.002	7401

Notes. [a] Dhooghe et al. (2017), October 2014.
[b] Weighted logarithmic average (WLA) for October 2014.
[c] WLA for the complete data set.
[d] WLA for data where $R_{HCl^+}/R_{CS_2^+} > 1.0$.
[e] WLA for Cl (complete data set) and HCl ($R_{HCl^+}/R_{CS_2^+} > 1.0$).

3.3.3. Chlorine-containing species on 67P

The R_{Cl+} /R_{HCl+} values from ^{35}Cl and ^{37}Cl are presented in Figure 13 and their ratios are summarized in Table 3. The following observations are made:

1 The observed $^{35}Cl^+/H^{35}Cl^+$ ratio varies throughout the mission in a way that closely resembles the CN/HCN ratio from (Hänni et al., 2020).

2 The full-mission value of 0.556 ± 0.031 for $^{35}Cl^+/H^{35}Cl^+$ differs from the one given by Dhooghe et al., 2017 for October 2014 due to differences in the data processing method and background correction applied.

3 The logarithmically weighted averages for $^{35}Cl^+/H^{35}Cl^+$ and for $^{37}Cl^+/H^{37}Cl^+$ differ by 1.9σ.

4 The full-mission ratios obtained for LEDA A and B are compatible with each other.

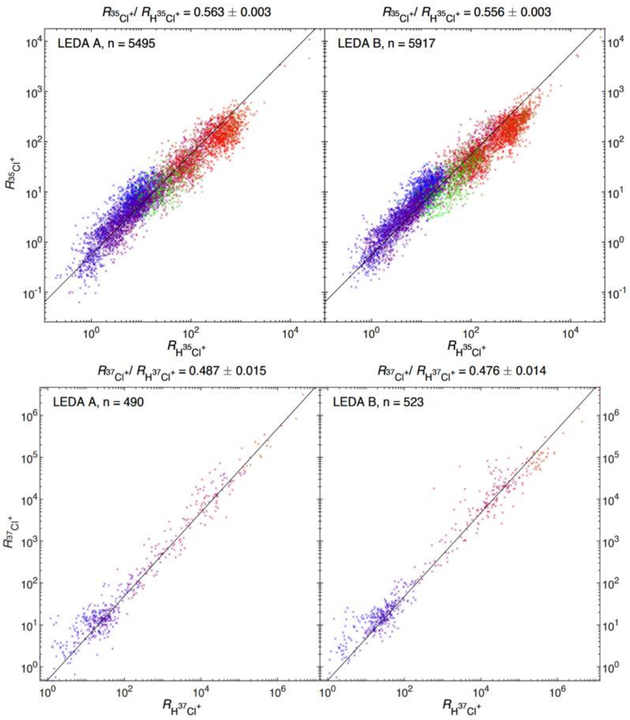

Figure 13: Upper panel: $R_{^{35}Cl^+}$ as a function of $R_{H^{35}Cl^+}$, lower panel: $R_{^{37}Cl^+}$ as a function of $R_{H^{37}Cl^+}$. The weighted logarithmic average ratio is given by the black line and its value and uncertainty are presented above the plot.

Table 3: Cl/HCl ratios obtained using integrated areas (R) and number of ions ($\mathcal{R}$) together with random (δR) and total ($\delta\mathcal{R}$) 1σ uncertainties and number of spectra used (n).

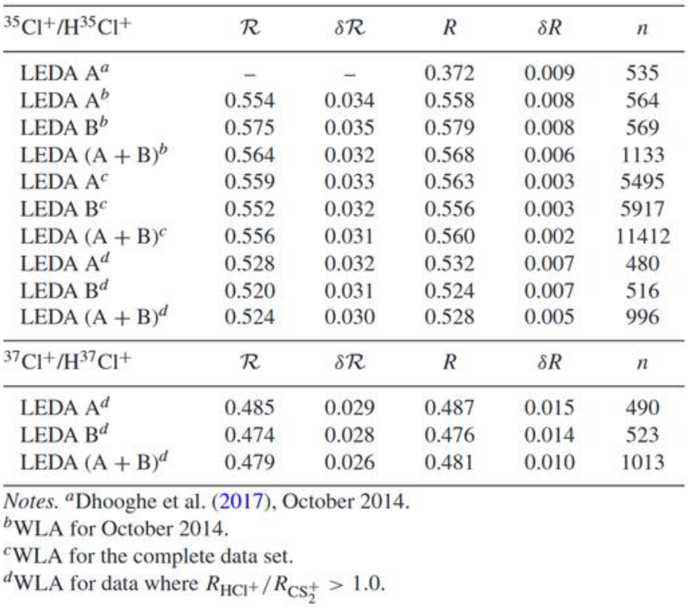

$^{35}Cl^+/H^{35}Cl^+$	$\mathcal{R}$	$\delta\mathcal{R}$	R	δR	n
LEDA A[a]	–	–	0.372	0.009	535
LEDA A[b]	0.554	0.034	0.558	0.008	564
LEDA B[b]	0.575	0.035	0.579	0.008	569
LEDA (A + B)[b]	0.564	0.032	0.568	0.006	1133
LEDA A[c]	0.559	0.033	0.563	0.003	5495
LEDA B[c]	0.552	0.032	0.556	0.003	5917
LEDA (A + B)[c]	0.556	0.031	0.560	0.002	11412
LEDA A[d]	0.528	0.032	0.532	0.007	480
LEDA B[d]	0.520	0.031	0.524	0.007	516
LEDA (A + B)[d]	0.524	0.030	0.528	0.005	996
$^{37}Cl^+/H^{37}Cl^+$	$\mathcal{R}$	$\delta\mathcal{R}$	R	δR	n
LEDA A[d]	0.485	0.029	0.487	0.015	490
LEDA B[d]	0.474	0.028	0.476	0.014	523
LEDA (A + B)[d]	0.479	0.026	0.481	0.010	1013

Notes. [a] Dhooghe et al. (2017), October 2014.
[b] WLA for October 2014.
[c] WLA for the complete data set.
[d] WLA for data where $R_{HCl^+}/R_{CS_2^+} > 1.0$.

Table 4: Cl⁺/HCl⁺ fragmentation ratios from literature

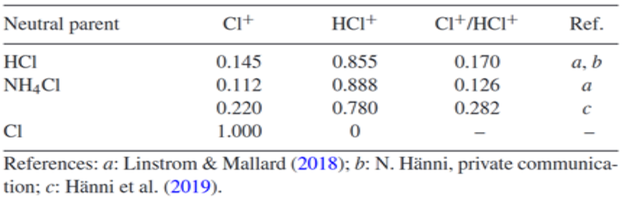

Neutral parent	Cl^+	HCl^+	Cl^+/HCl^+	Ref.
HCl	0.145	0.855	0.170	*a*, *b*
NH_4Cl	0.112	0.888	0.126	*a*
	0.220	0.780	0.282	*c*
Cl	1.000	0	–	–

References: *a*: Linstrom & Mallard (2018); *b*: N. Hänni, private communication; *c*: Hänni et al. (2019).

Cl^+/HCl^+ fragmentation ratios from literature (see Table 4) can assist in the identification of chlorine-bearing neutral parents. HCl (Dhooghe et al., 2017) and the ammonium salt NH_4Cl (Altwegg et al., 2020) were already known. However, the fragmentation patterns for both HCl and NH_4Cl are such that the corresponding Cl^+/HCl^+ ratios are considerably lower than the Cl^+/HCl^+ values found in the present analysis (see Table 3). This can only mean that there should be at least one other source of chlorine (XCl in what follows).

A few possibilities are explored for XCl:

- Cl: Although it seems unlikely due to its reactivity, the Cl radical itself is a candidate that cannot be excluded. For comparison, the CN radical was also discovered in the coma of 67P (Hänni et al., 2020).
- Other Cl-bearing species: Except for CH_3Cl (Fayolle et al., 2017), no other volatile Cl-bearing species have been identified in the DFMS mass spectra. As CH_3Cl is too low in abundance, this neutral is not a suitable neutral candidate to explain the observations. There is still a possibility for other Cl-bearing species to be present within the DFMS mass range at higher m_c/z, albeit with low abundances.
- Heavier semi-volatile Cl-bearing parents (C_xH_yCl) at higher m_c/z outside the DFMS mass range that sublimate and are present in the coma: These are improbable since the fragmentation of such parents in the DFMS ion source would also create Cl-bearing fragments at lower m_c/z and these are not observed.
- Compounds that decompose upon sublimation and/or ionization. As an example, it is known that ammonium perchlorate (NH_4ClO_4) releases HCl upon warming (Boldyrev, 2006). Other perchlorates or compounds with oxidized states of Cl may provide relatively more Cl^+ than HCl^+ upon dissociation.

These findings point to possible parents of the chlorine-bearing fragments that are not readily released from the nucleus and/or dust grains in the coma (semi-volatile species). Unfortunately, the identity of cometary semi-volatiles remains shrouded in mystery.

3.4. Improving mass calibration to allow the creation of sum spectra

To create sum spectra, individual spectra need to be mass calibrated (“aligned”) as perfectly as possible (preferably to within 0.1 pixel). A built-in DFMS feedback loop uses the measured magnet temperature to compensate for the temperature dependence of the magnet’s field strength. Still, large onboard temperature variations and other effects cause any given mass peak to move over a range of 30 pixels or more on the detector during the mission. Also note that on 27/01/2016 the ion beam was shifted to a less depleted zone of the detector in an effort to increase instrument sensitivity.

3.4.1. Introduction

The temperature-dependent pixel shift correction addressed in (De Keyser et al., 2019a) uses the pixel location where the maximum signal is found for CM 44 and shifts (aligns) these to the center detector pixel. The shift correction obtained this way is then used to align all CM. This approach is only valid provided the shift correction obtained at CM 44 is representative for the shift correction of all CM. This simple approach, however, was found to be insufficiently accurate to create sum spectra.

- *Ion beam shift*: The number of pixels shifted during the ion beam shift at 21/01/2016 is not the same for all CM. This is especially apparent for CM with a mass lower than 18.

- *Remaining data issues for CM 44*: data issue identification and removal were not automated and some data issues remained for CM 44. The shift correction cannot correctly be approximated for data with data issues and/or unexpected large pixel shifts. Also, the correction can never be better than what CM 44 allows.

- *Interpolation issues*: The maximum pixel location sometimes rapidly changes and interpolation of the data at CM 44 to other CM is not sufficiently accurate to align spectra.

The case of CM 44 was a particular case, as the pixel location of the peak with the maximum intensity always represents the pixel location of the main species on CM 44, i.e., CO_2. However, most spectra are not so straightforward: multiple peaks may be present in a spectrum, the peak with the maximum intensity may change over the course of the mission and sometimes no peak is found in the spectrum at all.

Part of the project therefore involved the development of a mass calibration process that is valid for the DFMS neutral high mass resolution mode measurements throughout the entire mission for the mass range m/z =13–69 and with an accuracy of less than a single pixel. This research was published in De Keyser et al. 2024 and the most important results will be presented here.

3.4.2. Data set

DFMS HR neutral measurements obtained near the comet between August 2014 and September 2016 are analysed. All spectra are interpolating to 0.1-pixel precision using cubic spline interpolation and an automated script determines the positions and intensity at the maximum for the 10 highest peaks for each spectrum and both detector channels. The smooth shape of the peaks allows to locate their positions consistently with a precision of 0.2 pixel or better. First the obtained information is used to identify and correct/remove spectra with issues.

DFMS mass peaks consist of two Gaussians centred at the same position, with the second Gaussian being broader and only at about 10% of the total peak intensity (N). Due to the

Poisson nature of the random incidence of ions on the detector, this double Gaussian peak shape can only be obtained when a sufficient number of ions is detected. The peak position is correct up to 1 pixel when at least 100 ions are counted and for lower ion counts the peaks are deformed and tend to have an off-nominal position because of low statistics. The peak position error can be estimated by $\delta p = \frac{100}{N} + 0.2\,\mathrm{pixel}$. In a second step, for each commanded mass-over-charge, a list of selected species is associated with the corresponding peaks. For a limited set of commanded mass-over-charge (m_c/z = 20, 24, 30, 32, 44), a spectrum-by-spectrum match of the masses with the 10 identified peaks yields an unambiguous identification. The result of this step is an assessment of how the peak position differs from the expected one as a function of time. This is then exploited to facilitate and accelerate the identification for all other peaks considered. For m_c/z = 16, 17, 18, for which V_{accel} was not stable, only data from the later part of the mission were used. The fragments in Table 5 represent the most abundant ones, whose positions are well-defined, while avoiding fragments that may be ambiguous. The selection is made in such a way that mistakes by the peak identification algorithm are minimized.

Possible misinterpretations can be identified when the peak position difference between both channels is too large (> 10 pixels) or when the deviation from the initial peak position time variation is too large (> 3 standard deviations from the running average). At least one useful peak has been identified for each m_c/z between 13 and 69 and only peaks with at least two ion counts per spectrum have been used.

In this way, one obtains for each spectrum its time t, the pixel positions p_A and p_B of the peaks on channel A and B, the peak intensities N_A and N_B, i.e., the number of ions incident on the MCP/LEDA during the 19.66 s acquisition time for each spectrum, and the peak position uncertainties δp_A and δp_B.

Table 5: Overview of main species in the mass calibration

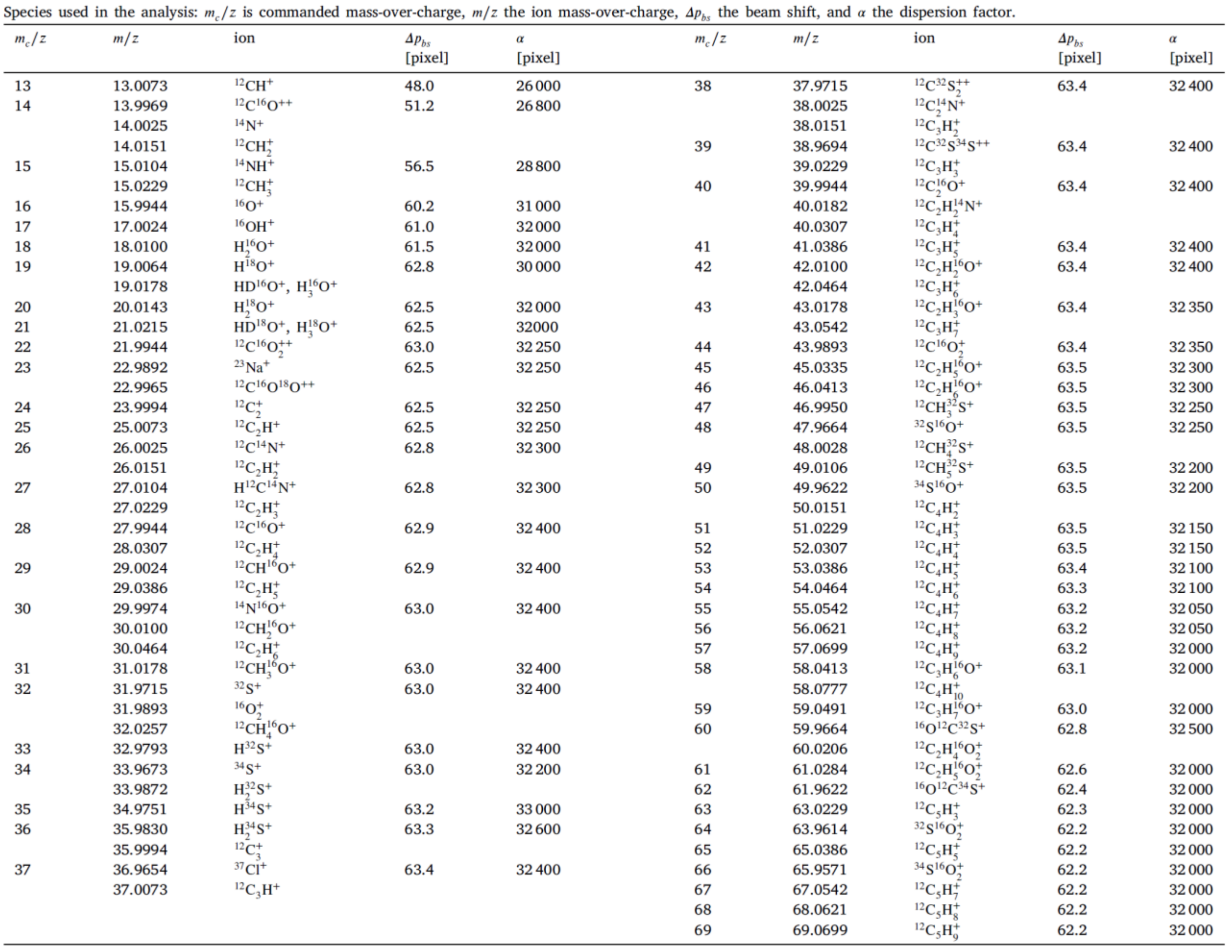

Species used in the analysis: m_c/z is commanded mass-over-charge, m/z the ion mass-over-charge, Δp_{bs} the beam shift, and α the dispersion factor.

m_c/z	m/z	ion	Δp_{bs} [pixel]	α [pixel]
13	13.0073	$^{12}\mathrm{CH}^+$	48.0	26 000
14	13.9969	$^{12}\mathrm{C}^{16}\mathrm{O}^{++}$	51.2	26 800
	14.0025	$^{14}\mathrm{N}^+$		
	14.0151	$^{12}\mathrm{CH}_2^+$		
15	15.0104	$^{14}\mathrm{NH}^+$	56.5	28 800
	15.0229	$^{12}\mathrm{CH}_3^+$		
16	15.9944	$^{16}\mathrm{O}^+$	60.2	31 000
17	17.0024	$^{16}\mathrm{OH}^+$	61.0	32 000
18	18.0100	$\mathrm{H}_2^{16}\mathrm{O}^+$	61.5	32 000
19	19.0064	$\mathrm{H}^{18}\mathrm{O}^+$	62.8	30 000
	19.0178	$\mathrm{HD}^{16}\mathrm{O}^+$, $\mathrm{H}_3^{16}\mathrm{O}^+$		
20	20.0143	$\mathrm{H}_2^{18}\mathrm{O}^+$	62.5	32 000
21	21.0215	$\mathrm{HD}^{18}\mathrm{O}^+$, $\mathrm{H}_3^{18}\mathrm{O}^+$	62.5	32000
22	21.9944	$^{12}\mathrm{C}^{16}\mathrm{O}_2^{++}$	63.0	32 250
23	22.9892	$^{23}\mathrm{Na}^+$	62.5	32 250
	22.9965	$^{12}\mathrm{C}^{16}\mathrm{O}^{18}\mathrm{O}^{++}$		
24	23.9994	$^{12}\mathrm{C}_2^+$	62.5	32 250
25	25.0073	$^{12}\mathrm{C}_2\mathrm{H}^+$	62.5	32 250
26	26.0025	$^{12}\mathrm{C}^{14}\mathrm{N}^+$	62.8	32 300
	26.0151	$^{12}\mathrm{C}_2\mathrm{H}_2^+$		
27	27.0104	$\mathrm{H}^{12}\mathrm{C}^{14}\mathrm{N}^+$	62.8	32 300
	27.0229	$^{12}\mathrm{C}_2\mathrm{H}_3^+$		
28	27.9944	$^{12}\mathrm{C}^{16}\mathrm{O}^+$	62.9	32 400
	28.0307	$^{12}\mathrm{C}_2\mathrm{H}_4^+$		
29	29.0024	$^{12}\mathrm{CH}^{16}\mathrm{O}^+$	62.9	32 400
	29.0386	$^{12}\mathrm{C}_2\mathrm{H}_5^+$		
30	29.9974	$^{14}\mathrm{N}^{16}\mathrm{O}^+$	63.0	32 400
	30.0100	$^{12}\mathrm{CH}_2^{16}\mathrm{O}^+$		
	30.0464	$^{12}\mathrm{C}_2\mathrm{H}_6^+$		
31	31.0178	$^{12}\mathrm{CH}_3^{16}\mathrm{O}^+$	63.0	32 400
32	31.9715	$^{32}\mathrm{S}^+$	63.0	32 400
	31.9893	$^{16}\mathrm{O}_2^+$		
	32.0257	$^{12}\mathrm{CH}_4^{16}\mathrm{O}^+$		
33	32.9793	$\mathrm{H}^{32}\mathrm{S}^+$	63.0	32 400
34	33.9673	$^{34}\mathrm{S}^+$	63.0	32 200
	33.9872	$\mathrm{H}_2^{32}\mathrm{S}^+$		
35	34.9751	$\mathrm{H}^{34}\mathrm{S}^+$	63.2	33 000
36	35.9830	$\mathrm{H}_2^{34}\mathrm{S}^+$	63.3	32 600
	35.9994	$^{12}\mathrm{C}_3^+$		
37	36.9654	$^{37}\mathrm{Cl}^+$	63.4	32 400
	37.0073	$^{12}\mathrm{C}_3\mathrm{H}^+$		
38	37.9715	$^{12}\mathrm{C}^{32}\mathrm{S}_2^{++}$	63.4	32 400
	38.0025	$^{12}\mathrm{C}_2^{14}\mathrm{N}^+$		
	38.0151	$^{12}\mathrm{C}_3\mathrm{H}_2^+$		
39	38.9694	$^{12}\mathrm{C}^{32}\mathrm{S}^{34}\mathrm{S}^{++}$	63.4	32 400
	39.0229	$^{12}\mathrm{C}_3\mathrm{H}_3^+$		
40	39.9944	$^{12}\mathrm{C}_2^{16}\mathrm{O}^+$	63.4	32 400
	40.0182	$^{12}\mathrm{C}_2\mathrm{H}_2^{14}\mathrm{N}^+$		
	40.0307	$^{12}\mathrm{C}_3\mathrm{H}_4^+$		
41	41.0386	$^{12}\mathrm{C}_3\mathrm{H}_5^+$	63.4	32 400
42	42.0100	$^{12}\mathrm{C}_2\mathrm{H}_2^{16}\mathrm{O}^+$	63.4	32 400
	42.0464	$^{12}\mathrm{C}_3\mathrm{H}_6^+$		
43	43.0178	$^{12}\mathrm{C}_2\mathrm{H}_3^{16}\mathrm{O}^+$	63.4	32 350
	43.0542	$^{12}\mathrm{C}_3\mathrm{H}_7^+$		
44	43.9893	$^{12}\mathrm{C}^{16}\mathrm{O}_2^+$	63.4	32 350
45	45.0335	$^{12}\mathrm{C}_2\mathrm{H}_5^{16}\mathrm{O}^+$	63.5	32 300
46	46.0413	$^{12}\mathrm{C}_2\mathrm{H}_6^{16}\mathrm{O}^+$	63.5	32 300
47	46.9950	$^{12}\mathrm{CH}_3^{32}\mathrm{S}^+$	63.5	32 250
48	47.9664	$^{32}\mathrm{S}^{16}\mathrm{O}^+$	63.5	32 250
	48.0028	$^{12}\mathrm{CH}_4^{32}\mathrm{S}^+$		
49	49.0106	$^{12}\mathrm{CH}_5^{32}\mathrm{S}^+$	63.5	32 200
50	49.9622	$^{34}\mathrm{S}^{16}\mathrm{O}^+$	63.5	32 200
	50.0151	$^{12}\mathrm{C}_4\mathrm{H}_2^+$		
51	51.0229	$^{12}\mathrm{C}_4\mathrm{H}_3^+$	63.5	32 150
52	52.0307	$^{12}\mathrm{C}_4\mathrm{H}_4^+$	63.5	32 150
53	53.0386	$^{12}\mathrm{C}_4\mathrm{H}_5^+$	63.4	32 100
54	54.0464	$^{12}\mathrm{C}_4\mathrm{H}_6^+$	63.3	32 100
55	55.0542	$^{12}\mathrm{C}_4\mathrm{H}_7^+$	63.2	32 050
56	56.0621	$^{12}\mathrm{C}_4\mathrm{H}_8^+$	63.2	32 050
57	57.0699	$^{12}\mathrm{C}_4\mathrm{H}_9^+$	63.2	32 000
58	58.0413	$^{12}\mathrm{C}_3\mathrm{H}_6^{16}\mathrm{O}^+$	63.1	32 000
	58.0777	$^{12}\mathrm{C}_4\mathrm{H}_{10}^+$		
59	59.0491	$^{12}\mathrm{C}_3\mathrm{H}_7^{16}\mathrm{O}^+$	63.0	32 000
60	59.9664	$^{16}\mathrm{O}^{12}\mathrm{C}^{32}\mathrm{S}^+$	62.8	32 500
	60.0206	$^{12}\mathrm{C}_2\mathrm{H}_4^{16}\mathrm{O}_2^+$		
61	61.0284	$^{12}\mathrm{C}_2\mathrm{H}_5^{16}\mathrm{O}_2^+$	62.6	32 000
62	61.9622	$^{16}\mathrm{O}^{12}\mathrm{C}^{34}\mathrm{S}^+$	62.4	32 000
63	63.0229	$^{12}\mathrm{C}_5\mathrm{H}_3^+$	62.3	32 000
64	63.9614	$^{32}\mathrm{S}^{16}\mathrm{O}_2^+$	62.2	32 000
65	65.0386	$^{12}\mathrm{C}_5\mathrm{H}_5^+$	62.2	32 000
66	65.9571	$^{34}\mathrm{S}^{16}\mathrm{O}_2^+$	62.2	32 000
67	67.0542	$^{12}\mathrm{C}_5\mathrm{H}_7^+$	62.2	32 000
68	68.0621	$^{12}\mathrm{C}_5\mathrm{H}_8^+$	62.2	32 000
69	69.0699	$^{12}\mathrm{C}_5\mathrm{H}_9^+$	62.2	32 000

A number of instrument temperatures are also obtained from the instrument housekeeping data. The heliocentric distance R and the solar aspect angle ψ between the spacecraft–Sun direction and the DFMS look direction are computed from the SPICE kernels. Figure 14 offers an overview of the data acquired for m_c/z = 32, good for about 14 200 spectra. Figure 14e shows the peak positions of the three main peaks at m_c/z = 32. The peak positions p_A and p_B recorded by channel A and B are slightly different, so that there are two slightly shifted curves for each mass peak.

The peak positions are seen to move collectively, and one can visually notice that these motions are related to the temperature variations. In early 2016 a ‘‘beam shift’’ was implemented by systematically reducing the acceleration voltage. This beam shift amounts to ∼63 pixels at m_c/z = 32. In general, the shifted peaks are found at

$$\tilde{p}_{A,B} = p_{A,B} + \Delta p_{bs}(m_c/z) \qquad \text{Eq. 7}$$

where $\Delta p_{bs}(m_c/z)$ is determined a priori by comparing the average peak positions immediately before and after the shift. For the remainder of this discussion, it is assumed that the beam shift has been applied.

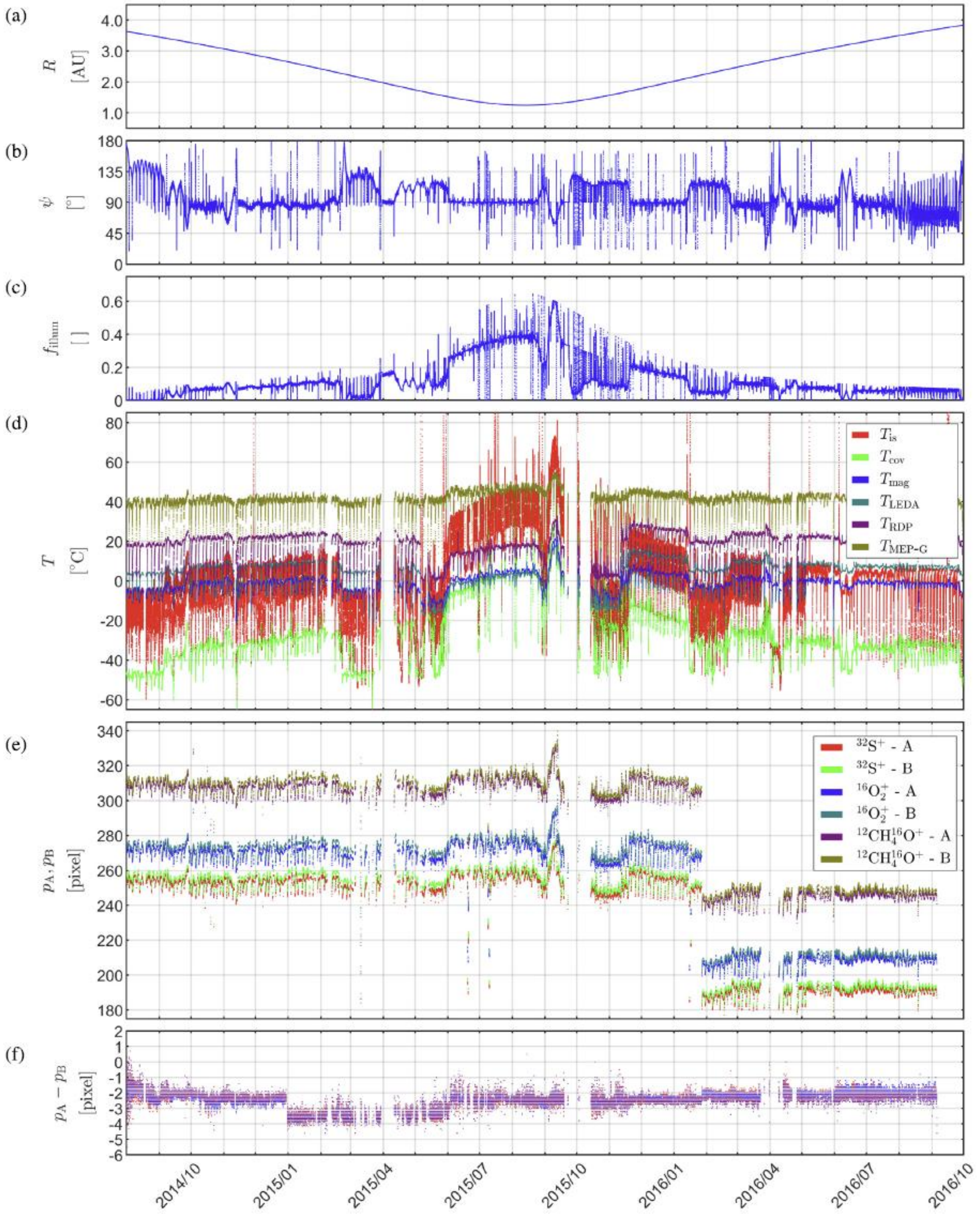

Figure 14: An overview of DFMS data used in this study: (a) distance from the Sun R, (b) solar aspect angle ψ, (c) the illuminated fraction of DFMS f_{illum}, (d) various DFMS temperature sensor readings, (e) pixel positions p_A and p_B of the 3 peaks in the $m_c/z = 32$ neutral mode HR spectra for both MCP/LEDA channels, and (f) their pixel difference $p_A - p_B$.

Figure 15 shows that the relative distributions of the differences between the positions of the three peaks remain within ±0.3 pixels from their average values, for each channel, again confirming that the peak position data set is accurate to 0.2 pixels and validating the use of sub-pixel precision.

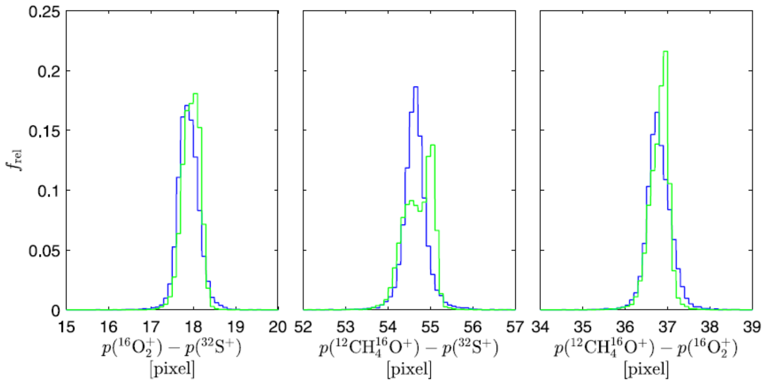

Figure 15: Probability distributions of the differences in position of the 3 peaks in the $m_c/z = 32$ mass spectra (blue for channel A, green for channel B).

3.4.3. Parameters affecting mass calibration

The actual mass calibration relation is more complicated than suggested by Eq. 1. Any non-ideal behaviour in the ion optics (acceleration behind the source slit, deflection in the electrostatic analyser and the magnet, dispersion in the zoom optics) modifies the relation. Moreover, the physical laws governing a mass spectrometer are continuous, while the control laws for operating the instrument work via the setting of electric potentials, limited to a discrete set of values. Therefore, although the mass calibration relation can theoretically be described by continuous laws, in practice the relation is a discrete one.

Magnetic fields: The magnet strength depends on its temperature T_{mag} according to:

$$B = 0.3550[\mathrm{T}] - 1.7262\times10^{-4}[\mathrm{T}/{\circ}\mathrm{C}](T_{mag} - 22.0)[{\circ}\mathrm{C}]. \qquad \text{Eq. 8}$$

DFMS features a feedback system that adapts V_{accel} based on the continuous measurement of T_{mag}. This feedback loop is meant to remove the effect of T_{mag} from the mass calibration relation. Unfortunately, a temperature dependence remains present. This is evident in Figure 16, which correlates the position of the $^{16}O_2^+$ peak in the $m/z = 32$ spectra from channel A (after correcting for the beam shift) to T_{mag}. There is a positive correlation at short time scales (variations related to instrument shutdown and cold restart). So, the uncertainty in temperature correlates with an uncertainty in pixel position.

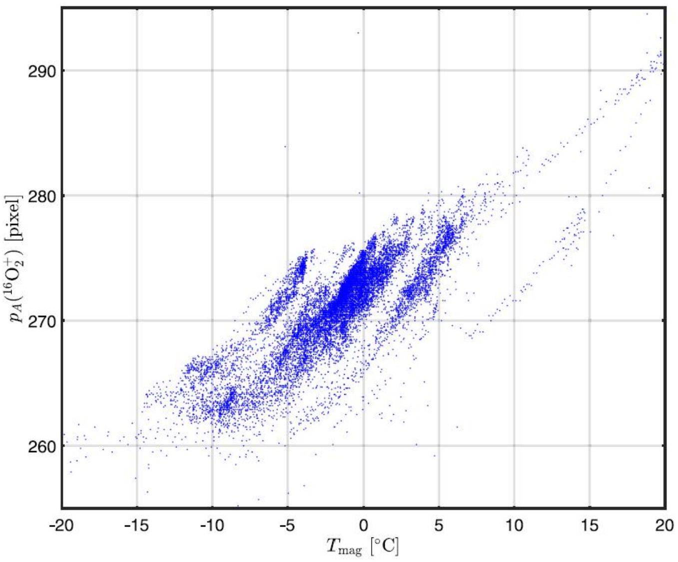

Figure 16: Correlation between the position of $^{16}O_2^+$ *in the* $m_c/z = 32$ *spectra (channel A after beam shift correction) and the magnet temperature* T_{mag}

Electric fields: The acceleration voltage is chosen so as to guide (hypothetical) ions with the commanded mass-over-charge onto the centre pixel, thereby attempting to compensate for the magnet strength variability. However, the precision with which the electric fields in the instrument can be set is finite. As a consequence, there will always remain some jitter in the peak positions.

Mechanical effects: Strong thermal gradients may exist across the optical tube despite the encapsulation in thermal blankets, which results in tube. Additionally, also the mounting of the zoom optics and other elements may be affected by temperature. Such thermal deformations may lead to stick–slip behaviour, i.e., discontinuous changes showing an unpredictable hysteresis effect with temperature. Another mechanical effect is the misalignment of the ion optics, responsible for the slight offset between mass peak positions on channels A and B. Asymmetric illumination can lead to a torsional deformation of the tube so that this misalignment and Δp_{AB} may change with temperature.

Effects in the ion source: Refractory dust material may cover part of the slit with a width of 14 µm used in high-resolution mode, similar to the typical size range of cometary dust particles, which will result in a reduction in instrument transmission and a displacement of the mass peak.

3.4.4. Methodology

The basic technique for computing the mass calibration from (De Keyser et al., 2019a) using the position of the well-defined and isolated CO_2^+ peak at $m_c/z = 44$ was expanded on and combined with the mass calibration relation of Eq. 2.

A temperature dependence Δp_T captures short-term variations in peak position. Any other short- or long-term variations due to mechanical effects or changing temperatures elsewhere in the instrument are captured by a function of time $D(t)$ that does not depend on m_c/z.

A term $\Delta p_0(m_c/z)$ covers the possibility that the commanded mass-over-charge position on the detector may depend on m_c/z instead of being exactly at the centre.

Because electric potentials are discrete, (small) additional corrections $\Delta p_{m_c/z}$ at each m_c/z are introduced.

The fact that Δp_{AB} changes slightly with m_c/z is accounted for through reliable measurements (i.e., for peaks with sufficiently high ion counts, spread over the entire mass range) of Δp_{AB}. The value of Δp_{AB} for other m_c/z is obtained by linear interpolation (first in time, thereafter in m_c/z).

This leads to mass calibration relations that are an extension of Eq. 2**Error! Reference source not found.**, giving the position of m/z as a function of time as

$$\begin{aligned}\hat{p}_A(m/z,t) = {} & p_0 + \alpha(m_c/z)\log\frac{m/z}{m_c/z} + \Delta p_0(m_c/z) + \Delta p_{m_c/z} \\ & + \Delta p_T(t) + \frac{1}{2}\Delta p_{AB}(t,m_c/z) + D(t),\end{aligned}$$

Eq. 9

$$\begin{aligned}\hat{p}_B(m/z,t) = {} & p_0 + \alpha(m_c/z)\log\frac{m/z}{m_c/z} + \Delta p_0(m_c/z) + \Delta p_{m_c/z} \\ & + \Delta p_T(t) - \frac{1}{2}\Delta p_{AB}(t,m_c/z) + D(t),\end{aligned}$$

Eq. 10

where m_c/z is the commanded mass-over-charge for the peak of mass m/z (the nearest integer mass-over-charge). The dispersion factor $\alpha(m_c/z)$, is computed for spectra in which multiple well-identified peaks are present and interpolated elsewhere.

The computational technique will not be addressed here, but all details can be found in (De Keyser et al., 2024).

3.4.5. Results

The strongest temperature correlation is found to be that with T_{mag}, but smaller correlations with T_{LEDA} and T_{is} contribute as well. The peak position shifts by 1 pixel for every °C of magnet temperature change, in addition to the temperature correction that is already built into the DFMS processing unit (about 16 pixels/°C). $\Delta p_0(m_c/z)$ varies over a few pixels at most, while smaller discrete $\Delta p_{m_c/z}$ are responsible for the deviation of observed positions.

Overall, for a total of about 850 000 mass spectra at 57 different m_c/z, about 705 000 data points have been used from a total of 1 260 000 potential peak positions (56%) belonging to 84 different fragments. The difference between both is mostly due to peaks that were not intense enough (especially at m/z = 21, 23 and > 60), deformed peaks at 16, 17, 18, and to failing peak identification.

Figure 17 presents a visual evaluation of the quality of the fit by displaying both the observed and the model positions. In order to make the figure readable, it focuses on a 10-day interval (1–11 November 2016) and just a few mass peaks. Peak positions are seen to vary during the cold restart after each DFMS shutdown. As temperatures first drop a bit more due to thermal inertia and then recover due to the heat generated by the electronics, the peak positions follow the same trend. The differences between the measured positions (squares/diamonds for channel A/B) and the solid lines (interrupted at data gaps) are small.

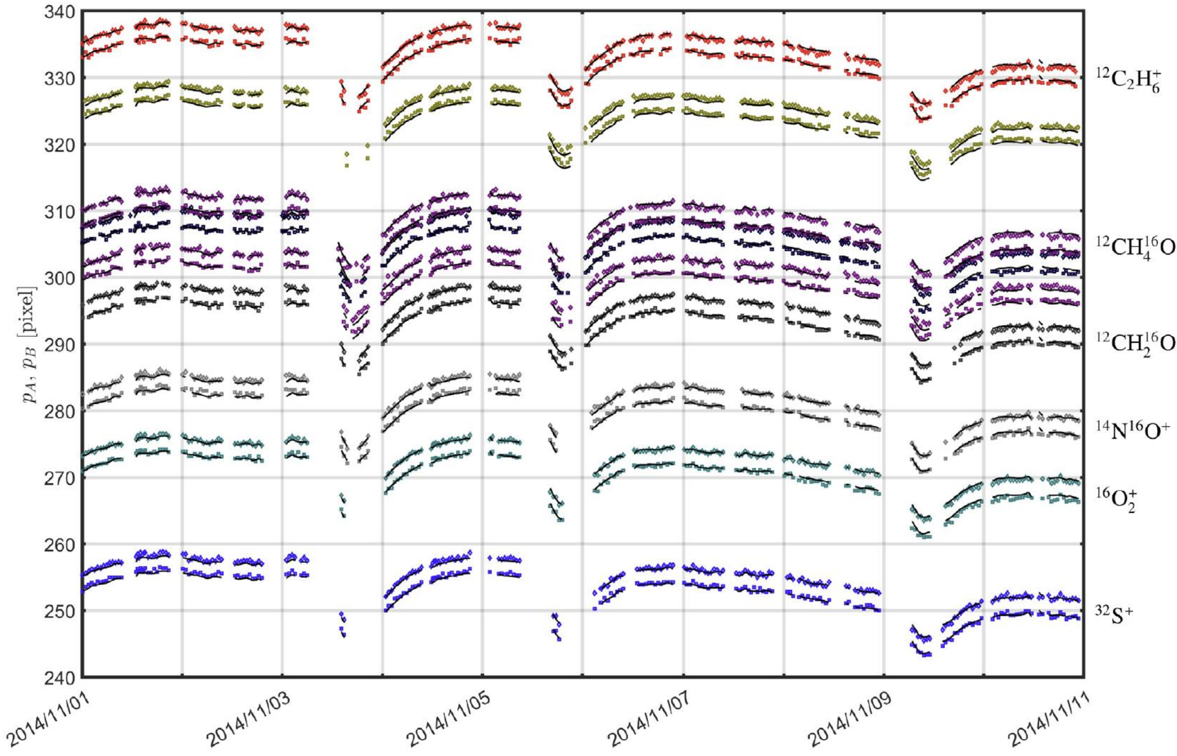

Figure 17: Observed peak positions p_A (squares) and p_B (diamonds) as well as model positions $\hat{p}_A$ and $\hat{p}_B$ (solid black line segments, interrupted where there are data gaps) for selected species at m⁄z = 30 and 32, during the first days of November 2014.

The same good fitting quality is achieved consistently throughout the entire mission and for all mass peaks (except at *m⁄z* = 16, 17, and 18 as discussed earlier).

Residuals for well-defined peaks are confined to ±1.0 pixel (∼3σ), sometimes with half of the distribution within ±0.2 pixel, the precision down to which the peak position data are given. Less abundant peaks have broader distributions, but still the bulk of the distribution is within ±1 pixel. The main reason for this is that the observed peaks are not necessarily at the nominal peak position because of the low count rates and the stochastic nature of the ion detection process (De Keyser et al., 2019b). Even smaller distribution widths can be obtained with a stricter data quality selection and outlier rejection.

3.4.6. Summary and conclusions

The optimization methodology fits a model of the peak positions observed in DFMS spectra in neutral high-resolution modes without post-acceleration to the data. The model considers variability due to temperature fluctuations on short time scales (associated with periodic instrument shutdowns) and on long time scales (associated with illumination changes and possibly thermal expansion/contraction). The model is valid for the entire comet encounter. The 1σ-precision is generally better than one pixel. Different explanations for the complex time-dependence have been discussed. The small residuals point to a common origin for the time variations captured by γ_{mag}, γ_{LEDA}, γ_{is}, and $D(t)$, regardless of m_c/z. The most likely explanation is that they result from temperature or thermomechanical effects and not from electric deviations, since the potential settings are different for the various m_c/z. The presence of dust near the slit, immediately downstream of the instrument ion source, may also explain part of the time variability. In conclusion, the physically motivated mass calibration relation presented here consolidates our understanding of DFMS behaviour in space. Having an accurate mass calibration is useful for facilitating fragment identification. One of the anticipated uses is in providing the correct common mass scale needed for producing sum spectra, which offer an improved signal-to-noise ratio.

While the mass calibration technique described here has been developed specifically for DFMS, it has more general applicability. Any type of mass spectrometer that employs a magnetic field must account for the change of magnetic field strength with temperature. A first approach is to use a thermostat to keep the magnet temperature within a narrow range. Such an approach may be limited by the thermal inertia of the instrument. Also, the operation of heaters might introduce undesirable temperature gradients within the magnet. In the case of mass spectrometers that combine a magnetic and an electric sector, like in the Nier–Johnson setup (Johnson and Nier, 1953), another way to cope with changing magnet strength is to compensate for it by adapting the electrostatic potentials in the instrument. However, there are limits on the precision of the magnet temperature measurement that drives this adaptation, and also the discretization of the electric field is a constraint. A third way to avoid magnet temperature problems is to alternate measurements of the sample with measurements of a reference sample with species at known nearby m/z to provide an experimental calibration. If any of these approaches (or a combination of them) fails to deliver a mass scale precision that is comparable to the mass resolution of the instrument, the technique described in this paper can be relevant, at least in situations where continuous measurements are made at different m/z: By identifying the main peaks and following their changing positions over time, the correlation with the temperature of the magnet and/or other parts of the instrument can be determined and the residual time dependence can be fitted in an ad hoc fashion. The usefulness of the approach lies in its being able to provide an accurate mass calibration for past measurements. Extrapolating the calibration to future measurements is only partially possible: One can use the temperature correlation, but the residual time dependence is not known in advance.

3.5. Sum spectra

Now that a procedure was created to align data to (mostly) within 1 pixel, sum spectra can be reliably created.

3.5.1. The creation of sum spectra

A sum spectrum is created by resampling each individual spectrum to 0.1 pixel using cubic spline interpolation and adding them together. Monthly spectra were created to search for lowly abundant ion species that are not always visible in the sum spectra. As an example, Figure 18 represents all monthly sum spectra for $m_c/z = 32$ and Figure 19 represents an overview of the individual spectra which compose the sum spectrum of July 2016.

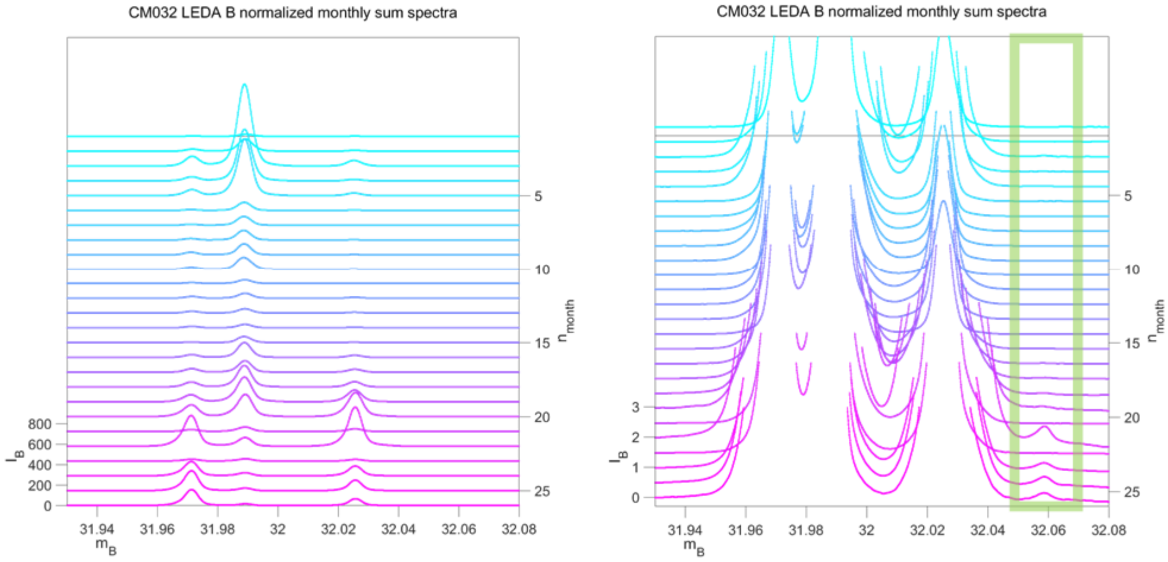

Figure 18: Left panel: monthly sum spectra for LEDA B for $m_c/z = 32$ between August 2014 ($n_{month} = 1$, blue) and September 2016 ($n_{month} = 25$, pink). Spectra are normalised to the single spectrum level. The spectra are vertically offset to allow an easy comparison between months. Right panel: Intensity zoom of the left panel between 0 and 3 counts/s to focus on lowly abundant species. A peak at m/z ~32.06 (possibly $^{13}C_2H_6$) is sometimes observed and given in green.

An additional peak, not clearly observable at the single spectrum level, is apparent in the sum spectra around *m*/*z* 32.06. This peak is very probably related to $^{13}C_2H_6$, an isotope of $^{12}C_2H_6$. This example illustrates that the mass calibration is very well defined for m_c/z 32. Similar sum spectra and overview graphs can be created for each m_c/z between 13 and 69.

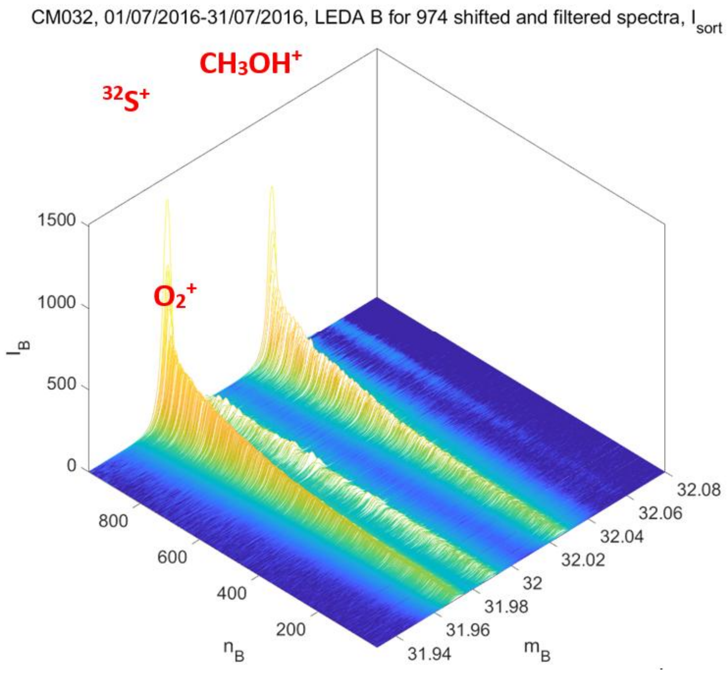

Figure 19: 3D overview of individual data from LEDA B for $m_c/z = 32$ *in July 2016. Spectra are normalised to the single spectrum level and sorted according to the peak with the largest intensity (here* $^{32}S^+$*). The species in the spectrum are identified in red above*

Some important caveats concerning the (direct) use of sum spectra for the identification of new species:

- The utmost care needs to be taken for the interpretation of sum spectra. For each and every additional/new peak in the sum spectra it needs to be verified that these peaks are not a result of issues at the single spectrum level (bad alignment, remaining data issues, …)
- Identification of related ions based on the mass is not always straightforward. The alignment of spectra at m_c/z with at least 1 abundant peak is generally within the desired accuracy and the mass scale is very well defined, which assists in limiting the number of possible candidates for a peak and can allow direct identification of an unknown peak. For spectra with no abundant peak, however, the alignment of spectra is less well-defined and more candidates can exist. Information from neighboring m_c/z can assist in the identification when isotopes are to be expected. Also note that doubly charged species exist in the spectra.
- Note that direct identification of lowly abundant species limits itself to species which can be mass-resolved using the instrument.

Because of these caveats, the investigation of all lowly abundant species in the sum spectra is not straightforward and not yet complete.

3.5.2. Identifying species from sum spectra

Using sum spectra, species for which the abundance is very low (not detectable at single spectrum level) and/or for which the abundance is variable across the mission have been detected. Some preliminary results are given in Table 6.

Table 6: Species detected in sum spectra at a given m_c/z; corresponding m/z where the peak is detected; abundance given as – : mostly not detectable at single spectrum level, or +: detectable at single spectrum level; and a tentative identification. Note that this list is incomplete.

m_c/z	*m/z*	**Abundance**	**ID (Tentative)**
14	13.988	+	$^{28}Si^{2+}$
15	14.998	-	NO^{2+} (or $C^{18}O^{2+}$)
18	18.044	-	Unknown
19	19.053	-	Unknown
20	19.980	-	$^{20}Ne^+$
24	23.985	+	$^{24}Mg^+$
27	26.971	-	Unknown
28	27.975	+	$^{28}Si^+$ (Rubin et al., 2017)
29	28.975	-	$^{29}Si^+$ (Rubin et al., 2017)
30	29.975	-	^{30}Si+ (Rubin et al., 2017)
31	30.975	+	Unknown ($H^{30}Si^+$?)
31	31.050	+	$^{13}CCH_6$
32	32.060	-	$^{13}C_2H_6$
34	34.040	-	$^{13}CH_5O$
35	34.994	-	HDS
36	35.968	+	$^{36}Ar^+$ (Balsiger et al., 2015)
37	36.966	+	$^{37}Cl^+$ (Dhooghe et al., 2017)
39	38.970	+	$C^{34}S^{32}S^{2+}$
40	39.995	+	C_2O^+
41	41.003	+	C_2HO^+
43	43.200	-	Unknown
46	46.055	-	Unknown
49	48.975	-	HSO^+
50	49.963	+	$^{34}SO^+$
52	52.006	-	$C_2N_2^+$
57	56.980	-	C_2HS^+
58	57.988	-	$C_2H_2S^+$
59	58.996	-	$C_2H_3S^+$
59	59.013	-	$C_2H_3O_2^+$
62	62.310	-	Unknown

Part of the species in Table 6 can be linked to surface sputtering (Wurz et al., 2015), are isotopes of more abundant species or are species that can be linked to the dust grain that entered the instrument on 5 September 2016 (Altwegg et al., 2017).

Refractory elements in the gas phase

Not only volatile species were found in the coma of 67P, but also refractory elements Na, Si, K, and Ca in the gas phase were reported early on in the Rosetta mission. Wurz et al., 2015 attributed the release of these species to sputtering by solar wind. One reason behind this notion was that their abundances were co-correlated but anti-correlated to the major gases in the coma. The total gas densities from the less active southern hemisphere early in the mission were consistent with a scenario of unhindered access on the part of the solar wind to the nucleus. The higher volatile densities above the simultaneously more active northern hemisphere resulted in a collisional attenuation of solar wind ion energies before reaching the surface. The derived relative abundances of Na/Si, K/Si, and Ca/Si were in agreement (Rubin et al., 2020) with the measured ratios in the cometary dust obtained by the COSIMA instrument (Bardyn et al., 2017).

The Si signal early in the mission, when Rosetta was close to the nucleus of 67P/C-G, was sufficient to obtain the ^{29}Si/^{28}Si and ^{30}Si/^{28}Si isotope ratios in the comet (Rubin et al., 2017). Both the ^{29}Si and ^{30}Si heavy isotopes were lower in abundance with respect to ^{28}Si when compared to the corresponding solar ratios. Refractory elements are well known to be present in the cometary dust phase. However, the same elements have also been identified in the gas phase: abundant amounts of Fe and Ni atoms were detected in the coma of about 20 comets, with some of them far away from the Sun (Manfroid et al., 2021). Up to that point, the corresponding emission lines of metallic atoms had only been observed in comets or exocomets that were either colliding with or passing close by the Sun or their host star, respectively.

The presence of refractory atoms in cometary comae over a range of heliocentric distances from <0.2 to >3 au sets constraints on the release processes, making these elements a key target of study. Research on refractory atoms in the coma of 67P has been published in Rubin et al., 2022, of which the authors of this report are co-authors.

Analysis of the m_c/z = 28 Da/e spectra in the coma of comet 67P/C-G revealed the presence of Si in the gaseous phase throughout the mission, covering the full range of heliocentric distances from 1.24 au to almost 4 au. Furthermore, Na has been identified, and occasional signals of Fe have been obtained near perihelion. Atomic Ni, on the other hand, was below the detection limit. This section summarizes these results and the conditions under which they were obtained.

Silicon (Si)

The stable isotopes of Si are found at m_c/z = 28–30 and an example set of spectra is seen in Figure 20. In the top panel, the major isotope ^{28}Si, identified by the black vertical line, is clearly visible in the left shoulder of CO, a major volatile in the coma of 67P. In the lower two panels, the low signals of the two minor isotopes, ^{29}Si and ^{30}Si, can be seen. There is a distinct absence of ^{28}SiH and ^{28}SiH$_2$ on m_c/z 29 and 30, respectively. As a result, silane and other Si-bearing species which fragment into SiH or SiH$_2$ are excluded as parent species.

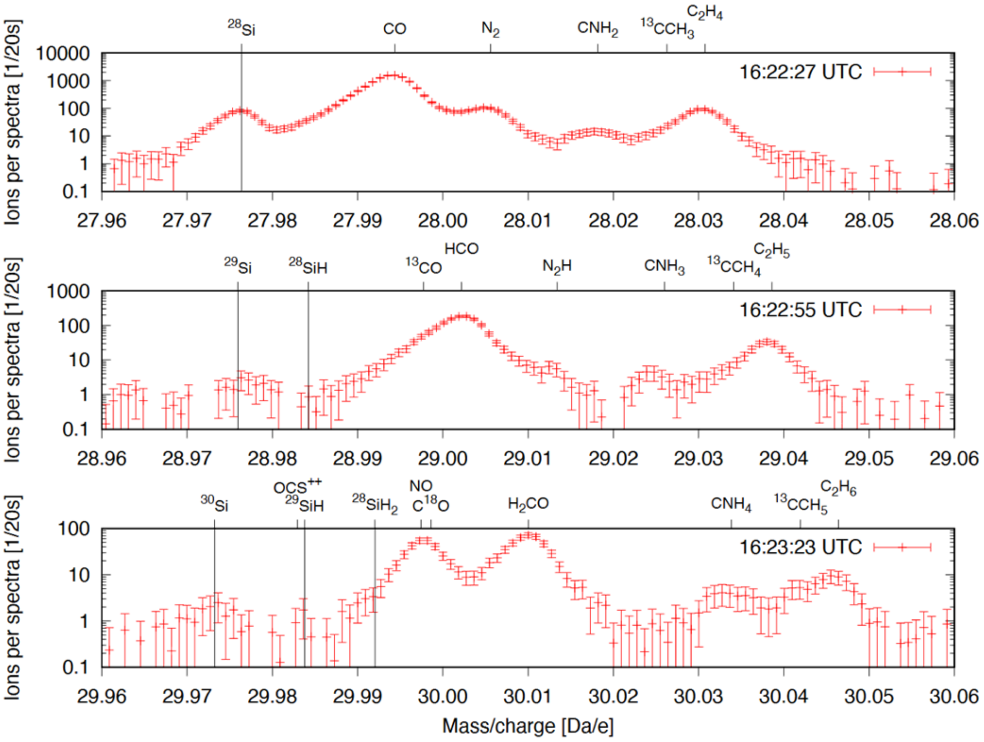

Figure 20: ROSINA DFMS m_c/z = 28 to 30 Da/e LEDA B spectra in log scale top to bottom, measured during the slew on 31 July 2015, at off-nadir angles decreasing from 150 to 148 degrees (see Fig. 26). Vertical lines mark the exact masses of species of interest, i.e., ^{28}Si with the minor isotopes ^{29}Si and ^{30}Si as well as where ^{28}SiH, ^{29}SiH, and ^{28}SiH$_2$ would be expected.

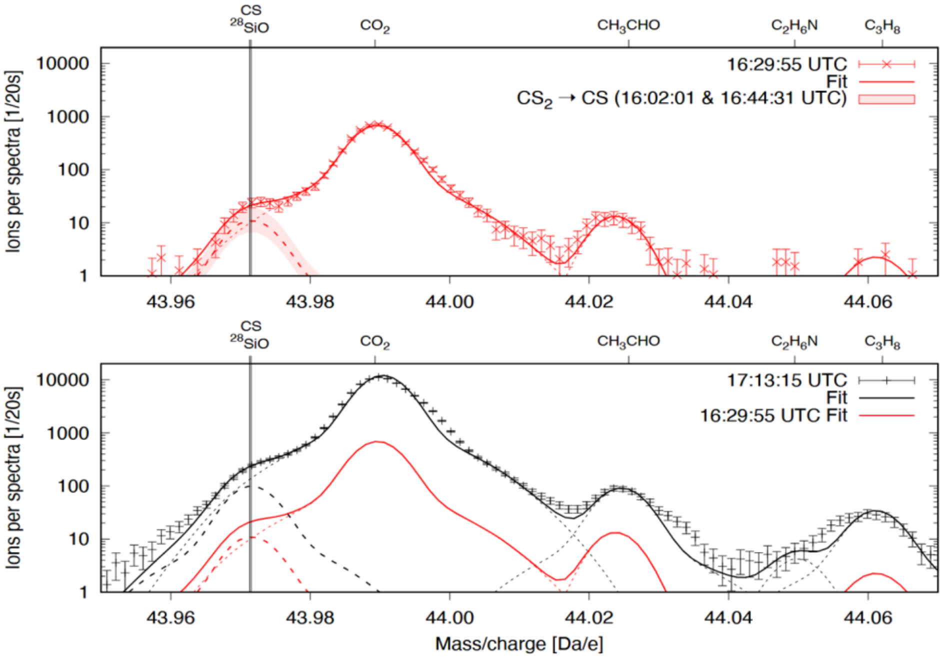

Figure 21: ROSINA DFMS m_c/z = 44 Da/e LEDA B spectra, measured on 31 July 2015 during and after the slew, at off-nadir angles 130 and 19 degrees, respectively. ^{28}SiO and CS cannot be separated and have been fitted as a single peak indicated by the red dashed line (dotted lines: all other species, solid line: sum curve). The contribution to CS by fragmentation of cometary parent CS$_2$ → CS is indicated by the red shaded area. The bottom panel also shows the sum curve of the upper panel for comparison.

Spectra in Figure 21 were obtained during a large slew, when the spacecraft was off-pointing from the nucleus. These conditions provide useful information on the origin of Si. Common volatiles found in 67P's coma are released from the nucleus and show a strong decrease in signal during these slews (almost a factor of ten), while Si, on the other hand, remained approximately constant.

The different behaviour of Si with respect to common volatiles indicates a much more uniform and extended distribution of atomic Si in the coma, possibly associated with a distributed source.

The detection of SiO is complicated by the almost identical mass of CS. CS is only formed by electron impact ionization of CS_2 in the ion source (Calmonte et al., 2016) and the signal at m_c/z 44 can be corrected for the contribution of CS using the abundance of CS_2 at m_c/z 76 and taking into account the $CS_2 \rightarrow CS$ fragmentation pattern. The fragmentation of CS_2 easily accounts for the full signal of the combined (CS+SiO) peak during the slew (Figure 21). The bottom panel of Figure 21 shows the spectrum just after the slew when DFMS was again pointing in the direction of the comet. The combined (CS+SiO) peak decreases by a factor of ~9, similarly to the common cometary volatiles such as CO_2 (~15) and C_3H_8 (~12), while Si (Figure 20), remained almost constant during that time. Both observations are evidence that the amount of SiO must be very small -if even present-.

Spectra at m_c/z = 40, 42, 56, 59, and 60 show no significant signal for SiC, SiN, Si_2, SiP, or SiS, respectively.

The relative signal strengths of ^{28}Si with respect to CO for the complete mission has been obtained from m_c/z = 28 spectra using the following corrections:

- The CO signal has been corrected for all fragment contributions (e.g., $CO_2 + e^- \rightarrow CO^+ + O + 2e^-$).
- The electron impact ionization cross-sections for Si and CO have been obtained from literature.
- CO^+ has been corrected for the fragmentation ratio of neutral CO into the CO^+ parent ion with respect to all ionized fragments produced ($CO + e^- \rightarrow CO^+ + 2e^-$ = 0.964 with only negligible amounts of CO^{2+}, C^+, and O^+).
- The instrument transmission is assumed to be the same for both species.
- The detection yield on DFMS' MCP detector is the same for both species.

The local densities of Si were estimated and combined with the densities of CO in Figure 22. Si was found to be present throughout the complete mission. Simultaneous variations of the CO and ^{28}Si densities are observed when the spacecraft moved to denser regions in the coma. The Si/CO ratio varied over the course of the mission, with a low ratio early and late in the mission at larger heliocentric distances and around peak activity. The fact that Si and CO were correlated at certain times (e.g., late 2015-early 2016) and not correlated at other times (e.g., early November 2014) shows that Si is of cometary origin and not associated with other effects such as spacecraft outgassing or the decomposition of spacecraft materials (Schläppi et al., 2010).

In terms of average local gas density, we obtained a median of the ratio of ^{28}Si/CO ~ 7 × 10^{-4} but with significant variations throughout the mission (see Figure 22). For the Si/H_2O ~ 2 × 10^{-5} ratio we use this median in combination with CO/H_2O = 3.1 × 10^{-2} from the pre-perihelion period or CO/H_2O = 3.0 × 10^{-2} time-integrated over the entire Rosetta mission and we neglect the higher mass isotopes, ^{29}Si and ^{30}Si.

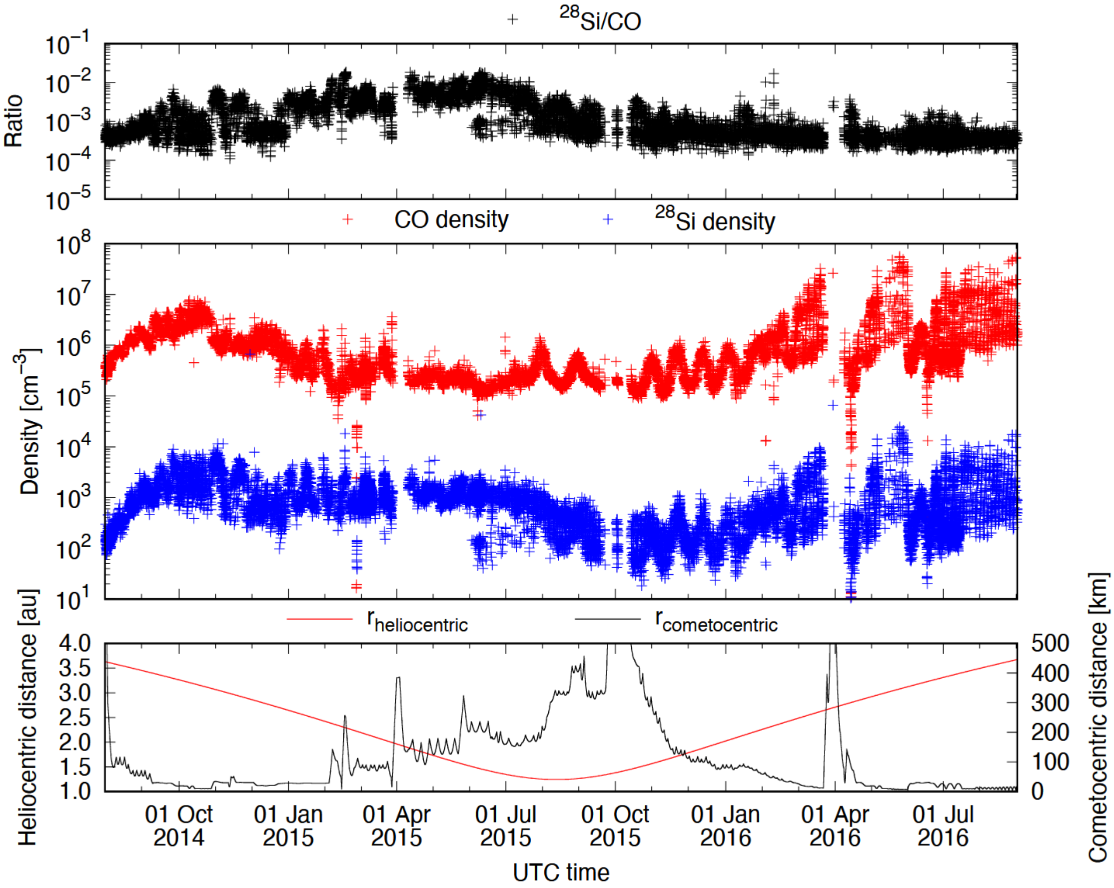

Figure 22: Timeline of the ^{28}Si/CO ratio (top panel) and individual CO and ^{28}Si densities (middle panel) measured in situ by ROSINA DFMS throughout the mission. The bottom panel shows the corresponding cometocentric distance of the Rosetta spacecraft and 67P/C-G's heliocentric distance.

Sodium (Na)

To evaluate the presence of Na, spectra at m_c/z = 23 Da/e have been investigated (see Figure 23). Na was found close to the peak activity of the nucleus, but count rates were generally low. Except for sometimes $^{12}C^{18}O^{16}O^{2+}$, very little interferences were observed. An analysis of the period from 26 to 29 July 2015 resulted in Na/Si ~ 0.16 when using the electron impact ionization cross-section for Na relative to Si and a mass-dependent sensitivity correction. Combined with Si/H_2O and neglecting minor Si isotopes follows Na/H_2O ~ 3 × 10^{-6} by number.

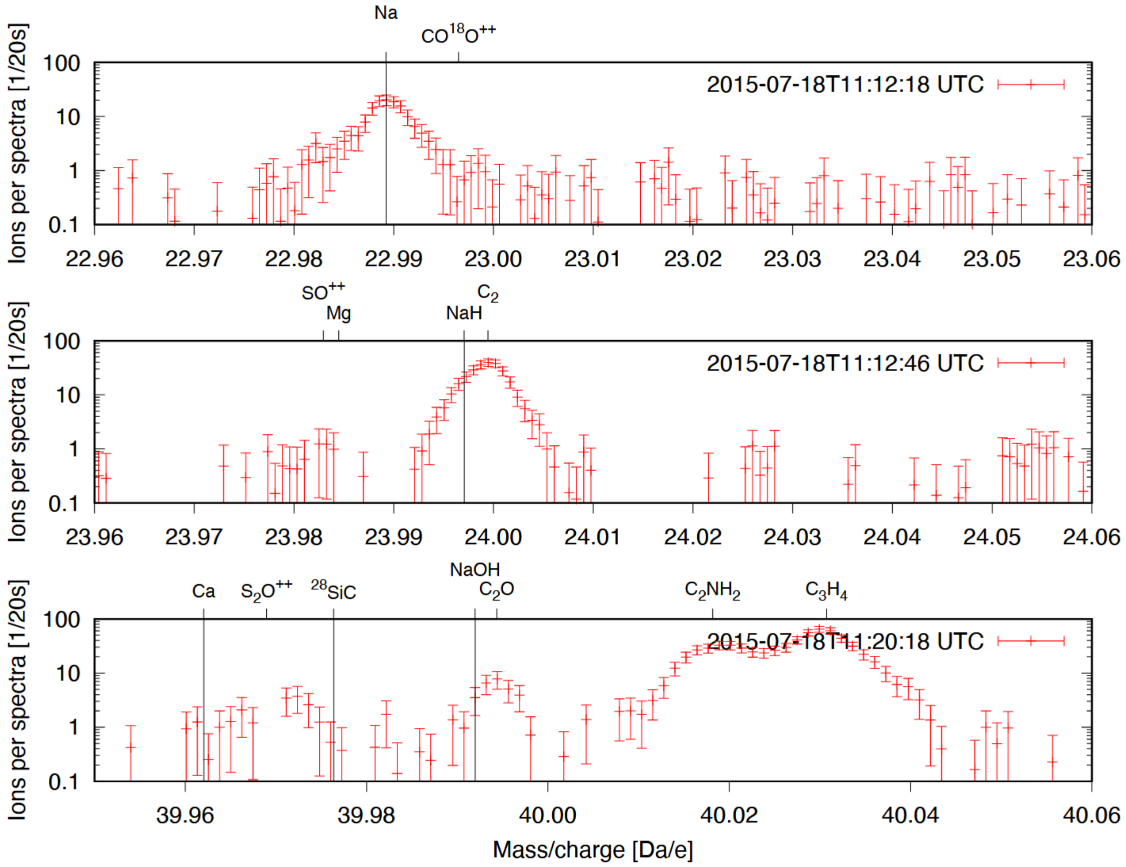

Figure 23: Top to bottom: ROSINA DFMS m_c/z = 23, 24, and 40 Da/e LEDA B spectra measured on 18 July 2015. Indicated are the masses of a several species including Na and where NaH and NaOH would be expected.

C_2 interferes with NaH (Figure 23, middle panel), the hydrated version of sodium at m_c/z = 24. The observed C_2 peak may mask small amounts of NaH. Given the asymmetric peak shapes found at these masses, a conservative limit of NaH/Na ≤ 1 can be found. At m_c/z = 40 (Figure 23, bottom panel) a small amount of NaOH may be hidden under the left shoulder of C_2O.

Iron (Fe) and Nickel (Ni)

Fe and Ni should be found at m_c/z = 56 and 58, respectively. Ni was not detected at m_c/z = 58 and spectra with hints of Fe are very rare. **Error! Reference source not found.** shows strong evidence for the presence of Fe in these few spectra.

Manfroid et al., 2021 proposed short-living parent molecules for Fe, among them carbonyls including iron pentacarbonyl $Fe(CO)_5$. FeCO at m_c/z = 84 is the major fragment of $Fe(CO)_5$, but was not found in the spectra. Also, no FeS was detected.

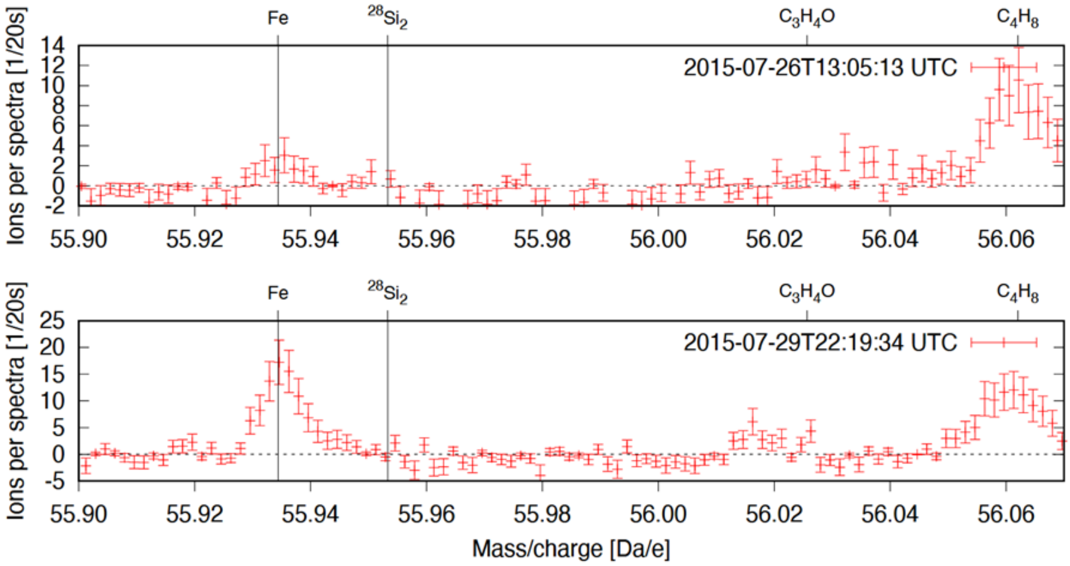

Figure 24: ROSINA DFMS m/Q = 56 Da/e spectra measured end July 2015 showing signals of Fe (top: row B; bottom: row A)

Summary and conclusions

In the previous section, a suite of detections and notable non-detections are reported. Their relative abundances or upper limits are collected in Table 7. These ratios have an uncertainty of up to a factor of ten due to small number statistics and possible fractionation effects given the limited volatility of the involved refractory species.

Table 7: Density ratios in the coma of 67P/C-G at Rosetta with respect to H_2O.

Ratio	Value	Analyzed period
Si/H_2O	$\sim 2 \times 10^{-5}$	Entire mission, Fig. 6
Na/H_2O	$\sim 3 \times 10^{-6}$	26–29 July 2015
Fe/H_2O	$\sim 5 \times 10^{-8}$	26–29 July 2015
Ni/H_2O	$<5 \times 10^{-8}$	26–29 July 2015

Table 8 recaps the upper limits on fragments that may be formed through 45 eV electron impact from larger parent molecules inside DFMS. These limits exclude, for instance, silane SiH_4, sodium hydroxide NaOH, or iron pentacarbonyl $Fe(CO)_5$ from being present near Rosetta in amounts relevant to explain the measured Si, Na, and Fe, respectively.

Table 8: Upper limits on fragments from 45 eV EI of larger Si-, Na-, and Fe-bearing parent and daughter molecules.

Element	Max ratio		
Na	NaH	≤	Na
	NaOH	≤	Na/5
Si	SiH	≤	Si/100
	SiH_2	≤	Si/50
	SiC	≤	Si/100
	SiN	≤	Si/100
	SiO	≤	Si/10
	Si_2	≤	Si/100
	SiP	≤	Si/100
	SiS	≤	Si/100
Fe	FeCO	≤	Fe
	FeS	≤	Fe

- The measurements revealed the presence of Si in the gas phase in the coma of comet 67P over a wide range of heliocentric distances. These observations show that sputtering by solar wind particles on the nucleus or near Rosetta, as identified early in the Rosetta mission, are unlikely the sole release process due to the collisional attenuation of the solar wind in the coma. However, based on our results, the transport of atoms sputtered from grains at increased cometocentric distances cannot be excluded.
- No parent molecules, or fragments thereof, for either Si, Na, or Fe, have been identified in our data set. Given the proximity to the nucleus of approximately 200 km, these observations favour the scenario that such elements are released directly from (nano)grains, rather than from a distributed source of gaseous parent molecules.
- Unlike common cometary volatiles, such as H_2O and CO_2, the Si signal remained stable when the spacecraft was off-pointing from the nucleus. Hence, (nano)grains in the coma are favored over grains on the nucleus' surface as source for the Si observed at the location of Rosetta.
- The release occurs most likely in atomic form, similar to S and the noble gases Ar, Kr, and Xe. Refractory-bearing parent molecules cannot be excluded; however, they would require scale lengths of << 200 km at a heliocentric distance of 1.25 au.

The question remains how exactly these refractory atoms end up in the gas phase and further studies are required to approach a credible answer.

4. SCIENTIFIC RESULTS AND RECOMMENDATIONS

As stated before, information on semi-volatile constituents in a comet can be derived only indirectly from Rosetta measurements as a function of cometary distance. Semi-volatile species can be identified by a progressive release from grains so their abundance in the coma relative to the abundance of volatile species increases as a function of distance from the comet.

A “distributed source” refers to the production of gaseous species in the coma from solid material (Cottin and Fray, 2008). These species are not directly released from the comet's nucleus but are instead generated through processes like the degradation of dust particles.

Semi-volatile species will always present as a distributed source within a defined distance from the comet. However, to be able to identify species as semi-volatile, we need to have sufficient information as a function of cometary distance within the range where not all semi-volatile has been released yet. Also note that not all distributed sources need to be semi-volatile; volatility is just one of the possible parameters which can result in a difference in release compared to the volatile species.

During the project, the following results have been obtained:

- Our studies on chlorine-bearing species point to possible parents of chlorine-bearing fragments that are not readily released from the nucleus and/or dust grains in the coma. Also, next to HCl and NH_4Cl, another chlorine-bearing species needs to be present to account for the observed additional Cl.
- Some of the lowly abundant species detected by DFMS can be linked to refractory elements (Si, Na or Fe). Si, for example is enhanced relative to common volatiles during off-pointing events which indicates a much more uniform and extended distribution of atomic Si in the coma, possibly associated with a distributed source. These are probably released directly from (nano)grains instead of from a distributed gaseous source.
- After a thorough optimization of DFMS mass calibration, sum spectra which contain very lowly abundant species are sometimes detected. Not all species could be uniquely identified up to now and a further detailed analysis is needed for a conclusive identification. Also, because of their low abundance, there is a very high probability that information is lacking to learn anything direct on possible release mechanisms.

The term “semi-volatile” may not have been the optimal name for the group of all species that are gathered by the definition given above as it inherently implies something about the volatility of the species. It is very unlikely that the observed distributed sources are exclusively linked to the volatility of species on grains. However, at this time it is not clear by which process refractory atoms end up in the gas phase. The release of species in a distributed source is most probably a delayed release from (nano)grains, for which the contribution of refractory elements like Si becomes more important the further away from the nucleus.

The creation of sum spectra has given us an additional tool to delve further in the data. Most of the species found could be linked to already known species or their isotopes. Unfortunately, not all discovered lowly abundant species have been conclusively identified yet and further research is needed on this topic.

Bibliography

Altwegg, K., Balsiger, H., Berthelier, J.J., Bieler, A., Calmonte, U., Fuselier, S.A., Goesmann, F., Gasc, S., Gombosi, T.I., Le Roy, L., De Keyser, J., Morse, A., Rubin, M., Schuhmann, M., Taylor, M.G.G.T., Tzou, C.-Y., Wright, I., 2017. Organics in comet 67P – a first comparative analysis of mass spectra from ROSINA–DFMS, COSAC and Ptolemy. Mon. Not. R. Astron. Soc. 469, S130–S141. https://doi.org/10.1093/mnras/stx1415

Altwegg, K., Balsiger, H., Hänni, N., Rubin, M., Schuhmann, M., Schroeder, I., Sémon, T., Wampfler, S., Berthelier, J.-J., Briois, C., Combi, M., Gombosi, T.I., Cottin, H., De Keyser, J., Dhooghe, F., Fiethe, B., Fuselier, S.A., 2020. Evidence of ammonium salts in comet 67P as explanation for the nitrogen depletion in cometary comae. Nat. Astron. 4, 533–540. https://doi.org/10.1038/s41550-019-0991-9

Balsiger, H., Altwegg, K., Bar-Nun, A., Berthelier, J.-J., Bieler, A., Bochsler, P., Briois, C., Calmonte, U., Combi, M., De Keyser, J., Eberhardt, P., Fiethe, B., Fuselier, S.A., Gasc, S., Gombosi, T.I., Hansen, K.C., Hässig, M., Jäckel, A., Kopp, E., Korth, A., Le Roy, L., Mall, U., Marty, B., Mousis, O., Owen, T., Rème, H., Rubin, M., Sémon, T., Tzou, C.-Y., Waite, J.H., Wurz, P., 2015. Detection of argon in the coma of comet 67P/Churyumov-Gerasimenko. Sci. Adv. 1, e1500377. https://doi.org/10.1126/sciadv.1500377

Balsiger, H., Altwegg, K., Bochsler, P., Eberhardt, P., Fischer, J., Graf, S., Jäckel, A., Kopp, E., Langer, U., Mildner, M., Müller, J., Riesen, T., Rubin, M., Scherer, S., Wurz, P., Wüthrich, S., Arijs, E., Delanoye, S., Keyser, J.D., Neefs, E., Nevejans, D., Rème, H., Aoustin, C., Mazelle, C., Médale, J.-L., Sauvaud, J.A., Berthelier, J.-J., Bertaux, J.-L., Duvet, L., Illiano, J.-M., Fuselier, S.A., Ghielmetti, A.G., Magoncelli, T., Shelley, E.G., Korth, A., Heerlein, K., Lauche, H., Livi, S., Loose, A., Mall, U., Wilken, B., Gliem, F., Fiethe, B., Gombosi, T.I., Block, B., Carignan, G.R., Fisk, L.A., Waite, J.H., Young, D.T., Wollnik, H., 2007. Rosina – Rosetta Orbiter Spectrometer for Ion and Neutral Analysis. Space Sci. Rev. 128, 745–801. https://doi.org/10.1007/s11214-006-8335-3

Bardyn, A., Baklouti, D., Cottin, H., Fray, N., Briois, C., Paquette, J., Stenzel, O., Engrand, C., Fischer, H., Hornung, K., Isnard, R., Langevin, Y., Lehto, H., Le Roy, L., Ligier, N., Merouane, S., Modica, P., Orthous-Daunay, F.-R., Rynö, J., Schulz, R., Silén, J., Thirkell, L., Varmuza, K., Zaprudin, B., Kissel, J., Hilchenbach, M., 2017. Carbon-rich dust in comet 67P/Churyumov-Gerasimenko measured by COSIMA/Rosetta. Mon. Not. R. Astron. Soc. 469, S712–S722. https://doi.org/10.1093/mnras/stx2640

Boldyrev, V.V., 2006. Thermal decomposition of ammonium perchlorate. Thermochim. Acta 443, 1–36. https://doi.org/10.1016/j.tca.2005.11.038

Calmonte, U., 2015. Sulfur Isotopic Ratios at 67P/Churyumov-Gerasimenko and Characterization of ROSINA-DFMS FM & FS.

Calmonte, U., Altwegg, K., Balsiger, H., Berthelier, J.J., Bieler, A., Cessateur, G., Dhooghe, F., Van Dishoeck, E.F., Fiethe, B., Fuselier, S.A., Gasc, S., Gombosi, T.I., Hässig, M., Le Roy, L., Rubin, M., Sémon, T., Tzou, C.-Y., Wampfler, S.F., 2016. Sulphur-bearing species in the coma of comet 67P/Churyumov–Gerasimenko. Mon. Not. R. Astron. Soc. 462, S253–S273. https://doi.org/10.1093/mnras/stw2601

Cottin, H., Fray, N., 2008. Distributed Sources in Comets. Space Sci. Rev. 138, 179–197. https://doi.org/10.1007/s11214-008-9399-z

De Keyser, J., Altwegg, K., Gibbons, A., Dhooghe, F., Balsiger, H., Berthelier, J.-J., Fuselier, S.A., Gombosi, T.I., Neefs, E., Rubin, M., 2019a. Position-dependent microchannel plate gain correction in Rosetta's ROSINA/DFMS mass spectrometer. Int. J. Mass Spectrom. 446, 116232. https://doi.org/10.1016/j.ijms.2019.116232

De Keyser, J., Dhooghe, F., Altwegg, K., Balsiger, H., Berthelier, J.-J., Briois, C., Calmonte, U., Cessateur, G., Combi, M.R., Equeter, E., Fiethe, B., Fuselier, S., Gasc, S., Gibbons, A., Gombosi, T., Gunell, H., Hässig, M., Le Roy, L., Maggiolo, R., Mall, U., Marty, B., Neefs, E., Rème, H., Rubin, M., Sémon, T., Tzou, C.-Y., Wurz, P., 2017. Evidence for distributed gas sources of hydrogen halides in the coma of comet 67P/Churyumov–Gerasimenko. Mon. Not. R. Astron. Soc. 469, S695–S711. https://doi.org/10.1093/mnras/stx2725

De Keyser, J., Dhooghe, F., Altwegg, K., Rubin, M., Hänni, N., Fuselier, S.A., Berthelier, J.-J., Neefs, E., 2024. Mass calibration of Rosetta's ROSINA/DFMS mass spectrometer. Int. J. Mass Spectrom. 504, 117304. https://doi.org/10.1016/j.ijms.2024.117304

De Keyser, J., Gibbons, A., Dhooghe, F., Altwegg, K., Balsiger, H., Berthelier, J.-J., Fuselier, S.A., Gombosi, T.I., Neefs, E., Rubin, M., 2019b. Calibration of parent and fragment ion detection rates in Rosettas ROSINA/DFMS mass spectrometer. Int. J. Mass Spectrom. 446, 116233. https://doi.org/10.1016/j.ijms.2019.116233

Dhooghe, F., De Keyser, J., Altwegg, K., Briois, C., Balsiger, H., Berthelier, J.-J., Calmonte, U., Cessateur, G., Combi, M.R., Equeter, E., Fiethe, B., Fray, N., Fuselier, S., Gasc, S., Gibbons, A., Gombosi, T., Gunell, H., Hässig, M., Hilchenbach, M., Le Roy, L., Maggiolo, R., Mall, U., Marty, B., Neefs, E., Rème, H., Rubin, M., Sémon, T., Tzou, C.-Y., Wurz, P., 2017. Halogens as tracers of protosolar nebula material in comet 67P/Churyumov–Gerasimenko. Mon. Not. R. Astron. Soc. 472, 1336–1345. https://doi.org/10.1093/mnras/stx1911

Dhooghe, F., De Keyser, J., Hänni, N., Altwegg, K., Cessateur, G., Jehin, E., Maggiolo, R., Rubin, M., Wurz, P., 2021. Chlorine-bearing species and the 37Cl/35Cl isotope ratio in the coma of comet 67P/Churyumov–Gerasimenko. Mon. Not. R. Astron. Soc. 508, 1020–1032. https://doi.org/10.1093/mnras/stab1732

Fayolle, E.C., Öberg, K.I., Jørgensen, J.K., Altwegg, K., Calcutt, H., Müller, H.S.P., Rubin, M., Van Der Wiel, M.H.D., Bjerkeli, P., Bourke, T.L., Coutens, A., Van Dishoeck, E.F., Drozdovskaya, M.N., Garrod, R.T., Ligterink, N.F.W., Persson, M.V., Wampfler, S.F., the ROSINA team, Balsiger, H., Berthelier, J.J., De Keyser, J., Fiethe, B., Fuselier, S.A., Gasc, S., Gombosi, T.I., Sémon, T., Tzou, C.-Y., 2017. Protostellar and cometary detections of organohalogens. Nat. Astron. 1, 703–708. https://doi.org/10.1038/s41550-017-0237-7

Glassmeier, K.-H., Boehnhardt, H., Koschny, D., Kührt, E., Richter, I., 2007. The Rosetta Mission: Flying Towards the Origin of the Solar System. Space Sci. Rev. 128, 1–21. https://doi.org/10.1007/s11214-006-9140-8

Hänni, N., Altwegg, K., Pestoni, B., Rubin, M., Schroeder, I., Schuhmann, M., Wampfler, S., 2020. First in situ detection of the CN radical in comets and evidence for a distributed source. Mon. Not. R. Astron. Soc. 498, 2239–2248. https://doi.org/10.1093/mnras/staa2387

Johnson, E.G., Nier, A.O., 1953. Angular Aberrations in Sector Shaped Electromagnetic Lenses for Focusing Beams of Charged Particles. Phys. Rev. 91, 10–17. https://doi.org/10.1103/PhysRev.91.10

Lai, I.-L., Ip, W.-H., Su, C.-C., Wu, J.-S., Lee, J.-C., Lin, Z.-Y., Liao, Y., Thomas, N., Sierks, H., Barbieri, C., Lamy, P., Rodrigo, R., Koschny, D., Rickman, H., Keller, H.U., Agarwal, J., A'Hearn, M.F., Barucci, M.A., Bertaux, J.-L., Bertini, I., Boudreault, S., Cremonese, G., Da Deppo, V., Davidsson, B., Debei, S., De Cecco, M., Deller, J., Fornasier, S., Fulle, M., Groussin, O., Gutiérrez, P.J., Güttler, C., Hofmann, M., Hviid, S.F., Jorda, L., Knollenberg, J., Kovacs, G., Kramm, J.-R., Kührt, E., Küppers, M., Lara, L.M., Lazzarin, M., Lopez Moreno, J.J., Marzari, F., Naletto, G., Oklay, N., Shi, X., Tubiana, C., Vincent, J.-B., 2016. Gas outflow and dust transport of comet 67P/Churyumov–Gerasimenko. Mon. Not. R. Astron. Soc. 462, S533–S546. https://doi.org/10.1093/mnras/stx332

Manfroid, J., Hutsemékers, D., Jehin, E., 2021. Iron and nickel atoms in cometary atmospheres even far from the Sun. Nature 593, 372–374. https://doi.org/10.1038/s41586-021-03435-0

Preusker, F., Scholten, F., Matz, K.-D., Roatsch, T., Willner, K., Hviid, S.F., Knollenberg, J., Jorda, L., Gutiérrez, P.J., Kührt, E., Mottola, S., A'Hearn, M.F., Thomas, N., Sierks, H., Barbieri, C., Lamy, P., Rodrigo, R., Koschny, D., Rickman, H., Keller, H.U., Agarwal, J., Barucci, M.A., Bertaux, J.-L., Bertini, I., Cremonese, G., Deppo, V.D., Davidsson, B., Debei, S., Cecco, M.D., Fornasier, S., Fulle, M., Groussin, O., Güttler, C., Ip, W.-H., Kramm, J.R., Küppers, M., Lara, L.M., Lazzarin, M., Moreno, J.J.L., Marzari, F., Michalik, H., Naletto, G., Oklay, N., Tubiana, C., Vincent, J.-B., 2015. Shape model, reference system definition, and cartographic mapping standards for comet 67P/Churyumov-Gerasimenko – Stereo-photogrammetric analysis of Rosetta/OSIRIS image data. Astron. Astrophys. 583, A33. https://doi.org/10.1051/0004-6361/201526349

Rubin, M., Altwegg, K., Balsiger, H., Berthelier, J.-J., Bieler, A., Calmonte, U., Combi, M., De Keyser, J., Engrand, C., Fiethe, B., Fuselier, S.A., Gasc, S., Gombosi, T.I., Hansen, K.C., Hässig, M., Le Roy, L., Mezger, K., Tzou, C.-Y., Wampfler, S.F., Wurz, P., 2017. Evidence for depletion of heavy silicon isotopes at comet 67P/Churyumov-Gerasimenko. Astron. Astrophys. 601, A123. https://doi.org/10.1051/0004-6361/201730584

Rubin, M., Altwegg, K., Berthelier, J.-J., Combi, M.R., Keyser, J.D., Dhooghe, F., Fuselier, S., Gombosi, T.I., Hänni, N., Müller, D., Pestoni, B., Wampfler, S.F., Wurz, P., 2022. Refractory elements in the gas phase for comet 67P/Churyumov-Gerasimenko - Possible release of atomic Na, Si, and Fe from nanograins. Astron. Astrophys. 658, A87. https://doi.org/10.1051/0004-6361/202142209

Rubin, M., Engrand, C., Snodgrass, C., Weissman, P., Altwegg, K., Busemann, H., Morbidelli, A., Mumma, M., 2020. On the Origin and Evolution of the Material in 67P/Churyumov-Gerasimenko. Space Sci. Rev. 216, 102. https://doi.org/10.1007/s11214-020-00718-2

Schläppi, B., Altwegg, K., Balsiger, H., Hässig, M., Jäckel, A., Wurz, P., Fiethe, B., Rubin, M., Fuselier, S.A., Berthelier, J.J., De Keyser, J., Rème, H., Mall, U., 2010. Influence of spacecraft outgassing on the exploration of tenuous atmospheres with in situ mass spectrometry. J. Geophys. Res. Space Phys. 115, 2010JA015734. https://doi.org/10.1029/2010JA015734

Scholten, F., Preusker, F., Jorda, L., Hviid, S., 2015. Reference frames and mapping schemes of comet 67P.

Schroeder I, I.R.H.G.S., Altwegg, K., Balsiger, H., Berthelier, J.-J., De Keyser, J., Fiethe, B., Fuselier, S.A., Gasc, S., Gombosi, T.I., Rubin, M., Sémon, T., Tzou, C.-Y., Wampfler, S.F., Wurz, P., 2019. ^{16} O/^{18} O ratio in water in the coma of comet 67P/Churyumov-Gerasimenko measured with the Rosetta/ROSINA double-focusing mass spectrometer. Astron. Astrophys. 630, A29. https://doi.org/10.1051/0004-6361/201833806

Wurz, P., Rubin, M., Altwegg, K., Balsiger, H., Berthelier, J.-J., Bieler, A., Calmonte, U., De Keyser, J., Fiethe, B., Fuselier, S.A., Galli, A., Gasc, S., Gombosi, T.I., Jäckel, A., Le Roy, L., Mall, U.A., Rème, H., Tenishev, V., Tzou, C.-Y., 2015. Solar wind sputtering of dust on the surface of 67P/Churyumov-Gerasimenko. Astron. Astrophys. 583, A22. https://doi.org/10.1051/0004-6361/201525980

5. DISSEMINATION AND VALORISATION

EGU2020-13051: Halogen-containing species at Comet 67P/Churyumov-Gerasimenko: Full mission results by F. Dhooghe, J. De Keyser, K. Altwegg, N. Hänni, M. Rubin, J.-J. Berthelier, G. Cessateur, M. Combi, S. Fuselier, R. Maggiolo and P. Wurz – Online poster session -

EGU21-10601: Chlorine-bearing species and the 37Cl/35Cl isotope ratio in the coma of comet 7P/Churyumov-Gerasimenko by F. Dhooghe, J. De Keyser, N. Hänni, K. Altwegg, G. Cessateur, E. Jehin, M. Rubin and P. Wurz – vPICO presentation-

Contribution to Dag van de wetenschap 2020: Bouw je eigen kometenjager

ESO Press-release #2108 on May 19, 2021 : “Heavy metal vapours unexpectedly found in comets throughout our Solar System — and beyond"; https://www.eso.org/public/news/eso2108/

EPSC2021-488, Dhooghe, F., De Keyser, J., Altwegg, K., Cessateur, G., Jehin, E., Maggiolo, R., and Rubin, M.: The next step for Rosetta ROSINA/DMFS data of comet 67P/Churyumov-Gerasimenko: the search for semi-volatiles species., Europlanet Science Congress 2021, online, 13–24 Sep 2021, https://doi.org/10.5194/epsc2021-488, 2021.

ULiège Press-release; https://www.lqj.uliege.be/cms/c_14592687/fr/du-lourd-dans-l-atmosphere-des-cometes, 15/09/2021

E. Jehin, J. Manfroid, and D. Hutsemékers. The discovery of Fe and Ni free atoms in comets atmospheres even far from the Sun. Oral presentation in AAS Division of Planetary Science meeting #53, id. 105.06. Bulletin of the American Astronomical Society, Vol. 53, No. 7 e-id 2021n7i105p06, online, 03-08 Oct 2021.

Contribution to “Dag van de wetenschap 2021”: Bouw je eigen kometenjager

EGU22-4474, Dhooghe, F., De Keyser, J., Hänni, N., Altwegg, K., Cessateur, G., Jehin, E., Maggiolo, R., Rubin, M., Wurz, P.: The search for low-abundant species in the coma of comet 67P/Churyumov-Gerasimenko, oral presentation in session PS5.1 – Small Bodies and Dust Open Session on Tuesday, 24 May 2022, 10:57 CEST

6. PUBLICATIONS

Dhooghe, F., De Keyser, J., Hänni, N., Altwegg, K., Cessateur, G., Jehin, E., Maggiolo, R., Rubin, M., Wurz, P., 2021. Chlorine-bearing species and the 37Cl/35Cl isotope ratio in the coma of comet 67P/Churyumov–Gerasimenko. Mon. Not. R. Astron. Soc. 508, 1020–1032. https://doi.org/10.1093/mnras/stab1732

Rubin, M., Altwegg, K., Berthelier, J.-J., Combi, M.R., Keyser, J.D., Dhooghe, F., Fuselier, S., Gombosi, T.I., Hänni, N., Müller, D., Pestoni, B., Wampfler, S.F., Wurz, P., 2022. Refractory elements in the gas phase for comet 67P/Churyumov-Gerasimenko - Possible release of atomic Na, Si, and Fe from nanograins. Astron. Astrophys. 658, A87. https://doi.org/10.1051/0004-6361/202142209

M. N. Drozdovskaya, I. Schroeder, M. Rubin, K. Altwegg, E. F. van Dishoeck, B. M. Kulterer, J. De Keyser, S. A Fuselier, M. Combi. Prestellar grain-surface origins of deuterated methanol in comet 67P/Churyumov–Gerasimenko. Monthly Notices of the Royal Astronomical Society, 500(4), 4901–4920, 2021. doi: 10.1093/mnras/staa3387

N. Hänni, K. Altwegg, H. Balsiger, M. Combi, S. A. Fuselier, J. De Keyser, B. Pestoni, M. Rubin, S. F. Wampfler. Cyanogen, cyanoacetylene, and acetonitrile in comet 67P and their relation to the cyano radical. Astronomy and Astrophysics, 647, A22, 2021. doi: 10.1051/0004-6361/202039580.

J. Manfroid, D. Hutsemékers, E. Jehin. Iron and nickel atoms in cometary atmospheres even far from the Sun. Nature, Volume 593, Issue 7859, p.372-374, 2021. doi: 10.1038/s41586-021-03435-0.

C. Opitom, E. Jehin, D. Hutsemékers et al. The similarity of the interstellar comet 2I/Borisov to Solar System comets from high-resolution optical spectroscopy. Astronomy & Astrophysics, Volume 650, id.L19, 8 pp., 2021. doi: 10.1051/0004-6361/202141245

D. Hutsemékers, J. Manfroid, E. Jehin, C. Opitom, and Y. Moulane. FeI and NiI in cometary atmospheres. Connections between the NiI/FeI abundance ratio and chemical characteristics of Jupiter-family and Oort-cloud comets. Astronomy & Astrophysics, Volume 652, id.L1, 7 pp. 2021. doi: 10.1051/0004-6361/202141554.

Rubin, M., Altwegg, K., Berthelier, J.-J., Combi, M.R., De Keyser, J., Dhooghe, F., Fuselier, S., Gombosi, T.I., Hänni, N., Müller, D., Pestoni, B., Wampfler, S.F., Wurz, P., 2022. Refractory elements in the gas phase for comet 67P/Churyumov-Gerasimenko - Possible release of atomic Na, Si, and Fe from nanograins. Astron. Astrophys. 658, A87. https://doi.org/10.1051/0004-6361/202142209

7. ACKNOWLEDGEMENTS

Work at BIRA-IASB was supported by the Belgian Science Policy Office via B2/191/P1/SeVoCo and PRODEX/ROSINA PEA90020 and 4000107705.

J. Manfroid., D.Hutsemékers. and E. Jehin. are Honorary Research Director, Research Director and Senior Research Associate at the Fonds de la Recherche Scientifique (F.R.S-FNRS), respectively.

Work at UoB was funded by the State of Bern, the Swiss National Science Foundation (200020_207312), and by the European Space Agency PRODEX Program.

The results from ROSINA would not be possible without the work of the many engineers, technicians, and scientists involved in the mission, in the Rosetta spacecraft, and in the ROSINA instrument team over the past 20 years whose contributions are gratefully acknowledged. Rosetta is an ESA mission with contributions from its member states and NASA.